FOILING SuMoth CHALLENGE

UniCa SAILING TEAM

UNICA
UNIVERSITÀ DEGLI STUDI DI CAGLIARI

Foiling SuMoth Challenge Stage 1 - 2024

DESIGN, MANUFACTURING & SUSTAINABILITY

sponsored by

11TH HOUR RACING

MARINESHIFT360

PERSICO

Bcomp

UNICASAILINGTEAM | UNIVERSITÀ DEGLI STUDI DI CAGLIARI, CAGLIARI, ITALY | sailingteam@unica.it

Summary

ABSTRACT

The UNICA Sailing Team embraced a new challenge in its career, launching our first boat MARIPOSA for the 2024 SuMoth Challenge. In response to growing environmental concerns, we committed to creating a Moth boat that would blend versatility and ecological consciousness while maintaining industrial manufacturing techniques. The project began in December 2023, and despite the limited available time, we had to tackle challenges related to uncertain forces, loads, and navigation conditions. By consulting industry experts and recognizing the importance of safety, we ensured that components were built with safety coefficients exceeding standard requirements, thus ensuring resilience against unforeseen challenges. In our inaugural year of competition, we made a large use of the upcycling technique to give new life to the dismissed part. This approach made us familiar with the components and comprehensively understand the necessary connections and junctions. Material selection was guided by versatile and sustainability-oriented research. Lastly, given our limited experience in the field, the sensor department focused on future prototypes through scientific research and the development of new technologies and sensors to optimize future performance without adding unnecessary bulk, providing sensitive data to enhance the overall design and capabilities of the boat.

LIST OF TABLES

LIST OF FIGURES

1 ENGINEERING AND DESIGN

1.1 Preliminary design

The initiation of the design process was characterized by uncertain forces and loads, which immediately directed us toward collaboration with industry experts. In this context, after a very preliminary design with simplified analytical models, finite element analysis played a crucial role, providing us with the necessary tools to evaluate and understand the complexity of our project. The importance of selecting the type of element, mesh density, and size, along with load and boundary conditions, cannot be underestimated. These are fundamental elements to ensure the accuracy and efficiency of our structural analyses. Concurrently, the use of finite volume analysis within the OpenFoam code represents an additional valuable resource for evaluating the aerodynamic performance of our components. This method, based on the numerical discretization of governing equations, provides a detailed and accurate overview of the aerodynamic behavior of the main components of the boat. In this preliminary introduction, we explore the initial challenges faced during the design phase and emphasize the crucial importance of the tools utilized.

1.2 Hull Design

The design choices made stem from thorough analysis and thoughtful decision-making processes. Several factors were considered, including the environmental impact of materials, structural strength of the vessel, energy efficiency and speed of the construction methodology. Regarding the hull shape, the opportunity arose to use a MantaMoth mould as a production waste, which no longer met high-quality standards to produce new vessels. However, since it was not completely compromised, it still retained its shape and basic structure, offering us a unique opportunity to reuse an existing material rather than create a new one, thus reducing the overall ecological footprint of our construction. The mold came from a freelance boat builder and was used in their production activity for the creation of a series of racing boats. The mold, fabricated in 2017, is made out of glass fiber covered by carbon fiber, first of which is a composite material that is easy to work with, which can be molded to fit the creation of complex shapes, and whose surface finish is ideal for use as it is smooth and uniform. Furthermore, mold reuse allowed us to give a second life to a material otherwise destined for the landfill, demonstrating the potential of recycling and upcycling practices in the industry. Initially, upon examining the mold shape, it was necessary to identify areas requiring adjustments to modify the hull shape given the difference between the original MantaMoth wings and our new wings. To fill the voids in the original mold wings, a wooden filler core was fabricated to provide the necessary support for creating the wings designed by our team. Using CAD software, we replicated the hull shape and employed modeling techniques to adapt the shape to the specific requirements. Once the CAD design was completed, an industrial CNC machine at our university's DICAAR laboratories was utilized to produce the filler core. This process ensured high precision and exact correspondence to the intended shape (see Figure 2).

Figure 1: Mould's Shape

Figure 2: Mould's shape with wooden filler core

1.2.1 Material Selection of the Hull

The choice of hull material was deduced from a careful evaluation of the available resources, opting for the use of a composite material with flax fiber reinforcement and a PET core. This decision was driven by the desire to combine the mechanical, density, and strength properties of flax fiber and PET.

In the design process, the analysis of the mechanical properties of the used composite material was fundamental. To obtain an accurate assessment, we conducted several flexural fracture tests on samples with different configurations to determine the distinctive mechanical characteristics of each sample. Four different configurations were examined based on the presence or absence of a layer of flax fiber oriented at 0/90 [TWILL], which was placed externally to the layer oriented at +45/-45 [BIAX], and the thickness of the PET core. The elastic modulus of both configurations is reported in Table 1.

Flax Fiber [BIAX]	*61*	GPa
Flax Fiber [TWILL]	*62*	GPa

Table 1: Young's Modulus Flax Fiber

The tests revealed significant differences in the mechanical properties of the various samples. It was found that the insertion of the [TWILL] layer improved the flexural strength of the samples. Additionally, a significant result emerged regarding delamination failures in the samples with a 10 mm PET layer. Delamination occurs when different layers of the composite material separate, compromising cohesion and consequently the overall strength of the sample. In contrast, in samples with a 5 mm PET layer, no evidence of delamination was observed, although they exhibited classic flexural failure characterized by deformation and material fracture. The presence of delamination in samples with a 10 mm PET layer suggests that excessive thickness may compromise structural integrity.

Figure 3: Bending test with delamination

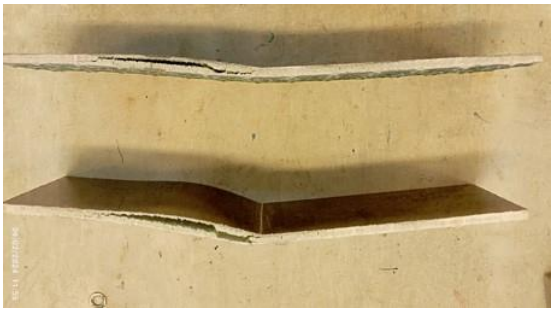

Figure 4: Samples with delamination failure

Figure 5: Bending test with no - delamination

Figure 6: Sample with bending failure

The results of the flexural test are reported in Table 2.

Composition	σ $[MPa]$	*Density [kg/m³]*
WL200/XL350/PET5/XL350/PR	*88,90*	*672*
WL200/XL350/PET10/XL350/PR	*49,90*	*480*
XL350/PET5/XL350/PR	*72,80*	*630*
XL350/PET10/XL350/PR	*46,00*	*429*

Table 2: Results of the flexural test

After carefully considering the results of the flexural tests (see Table 2), an optimal stratigraphy selection was made for the hull construction.

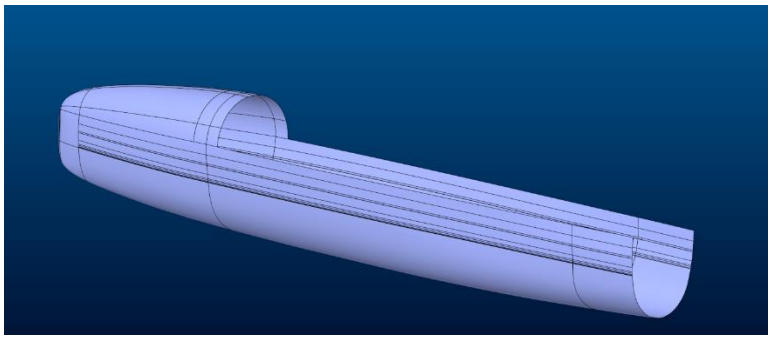

Figure 7: Hull surface

1.2.2 Bulkheads

In the design of the hull skeleton, the bulkheads are key element. Indeed, they play a fundamental role in the overall structure, see Figure 8. The bulkheads have been designed to provide structural strength and stability to the hull, considering various options of materials and configurations to achieve the desired performance. The bulkhead design process began with consultation with industry experts and analysis of technical datasheets of PVC sheets available in the market, providing an initial thickness value typically used in the creation of frames. This preliminary phase allowed for acquiring detailed information about the characteristics and performance of the available materials, providing a solid foundation for selecting the most suitable components for the construction of the hull bulkheads. Considering that the original up-cycled mould was designed for a composite CFRP (Carbon Fiber Reinforced Polymers) hull and bulkheads we tried to replicate the same mechanical properties, using more sustainable materials like wood reinforced with Kevlar. Using dedicated calculation tools (1), the mechanical properties of the composite were determined and reported in Table 3 , including the longitudinal and transverse elastic modulus, shear modulus, and stiffness matrix.

[BIAX/PVC5/BIAX]		
E_{xx}	25,43	GPa
E_{yy}	21,79	GPa
ν_{xy}	0,298	-
G_{xy}	1,47	GPa

Table 3: [BIAX/PVC 5 mm / BIAX]

Subsequently, through the objective function research, the mechanical characteristics of various types of wood, such as Balsa, Paulownia, and Marine Okoumé (marine plywood), were analyzed (2). The main objective was to identify the minimum thickness of wood for each type, integrating Kevlar reinforcement skins, to achieve comparable or at least similar performance to that of the reference composite bulkhead [BIAX/PVC/BIAX] used for the commercial MantaMoth, see Table 3. The mechanical properties for our configuration of the bulkheads that compared the CFRP properties are reported in Table 4.

[BIAX/OKUME6/BIAX]		
E_{xx}	22,50	GPa
E_{yy}	18,30	GPa
ν_{xy}	0,332	-
G_{xy}	6,05	GPa

Table 4: [BIAX/OKUME 6 mm/BIAX]

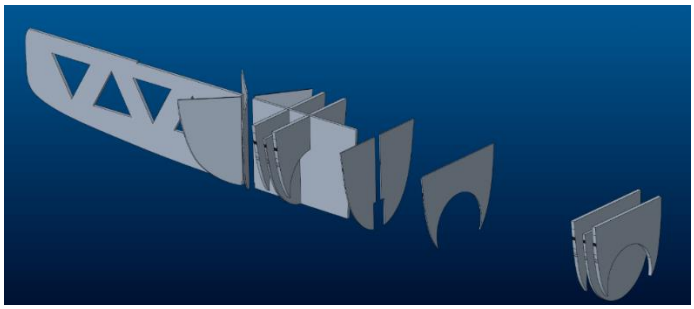

Figure 8: Bulkheads surface

Based on the gathered information, various design options were evaluated, considering the trade-offs between strength, weight, and cost. The primary objective was to identify the optimal solution that could ensure the desired performance while simultaneously

minimizing the impact on the total weight of the hull and on the environment.

1.3 Transom and Gantry

A critical aspect is represented by the construction of the transom, which has the main objective of providing a solid anchoring point for the gantry while ensuring the necessary strength and durability to withstand the aerodynamic forces from the rudder. Before proceeding with the detailed design of the transom, a preliminary analysis was conducted to evaluate the stresses it undergoes during operation. This analysis was performed using CFD software, which allowed simulation of the airflow behavior around the rudder and adjacent parts of the hull. Below are the results obtained from the CFD analysis (see Table 5, Table 6).

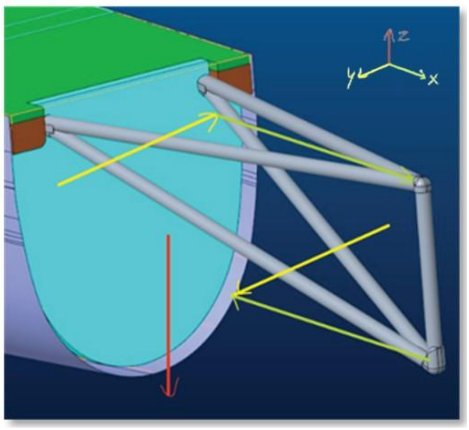

Figure 9: Stress Analysis

	$F_x\ [N]$	$F_y\ [N]$	$F_z\ [N]$
LOWER PART	3492.48	212.16	1599
UPPER PART	2850.48	173.16	1599

Table 5: Forces on the upper part

	$F_x\ [N]$	$F_y\ [N]$	$F_z\ [N]$
LOWER PART	3492.48	212.16	1599

Table 6: Forces on the lower part

Through an iterative process, see

Figure 9, these results were used to size and design the transom to ensure sufficient strength to withstand the service forces. To meet the strength requirements for the transom, it emerged that the upper part of the gantry anchored to the hull needs to reinforce the hull itself through a gradual increase in thickness, ensuring adequate strength capacity against the stresses induced during the service sail condition.
CFD analyses and structural simulations allowed the determination of the minimum thickness of the hull, and through a reflow check, the minimum area of connections was determined. This enabled accurately defining the dimensions and shape of the connections, ensuring a uniform distribution of stresses and a secure connection between the two components. In parallel with the analysis conducted for the upper part of the gantry, a similar analysis was carried out to determine the necessary area of the anchorage for the lower part, also considering the transfer of stresses through the lower point.

1.4 CFD Analysis of Hull and Sail

A comprehensive study on the aerodynamics of the entire vessel has allowed meeting the design requirements established by the Structures department. Based on the

indications provided by the skipper, three main sailing angles were identified: Beating, Reaching, and Running. For each of them, the position of the boat relative to the apparent wind and the boat speed were determined a priori.
The CFD analyses were performed using the open-source software OpenFOAM®, through which the aerodynamic flow was solved, and the acting forces on the sail and the loads on the terraces were derived. The latter were provided to the Structures department for structural verification.

1.4.1 Preliminary study of velocity Components of a Sailing Vessel

Based on the approximate polar diagram (3) shown in Figure 10 representing an ideal configuration for a competition moth, the forward velocity U_F was derived as a function of the sailing angle and true wind speed TWS. In this way, the apparent wind speed velocity (AWS) and the corresponding angle (AWA) are determined, according to the vectorial scheme depicted in Figure 11.

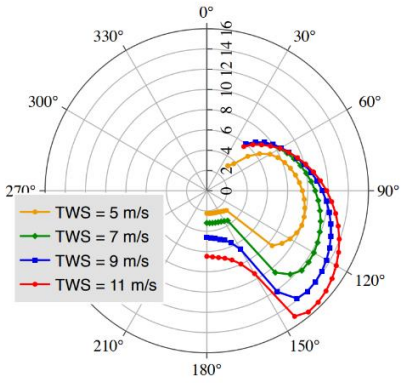

Figure 10: Polar Velocity Diagram

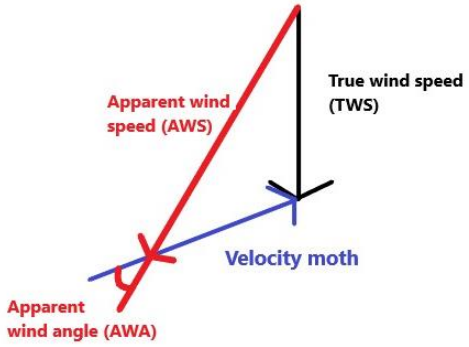

Figure 11: Diagram representing the different velocities composing the one acting on the moth in the reference system moving with the boat

Considering also the structural design, a $TWS = 11\ m/s$ has been chosen, representing the most critical wind condition in the polar velocity diagram. The previously mentioned numerical data are reported in Table 7.

	$TWS\ [m/s]$	$TWA\ [°]$	$U_F\ [m/s]$	$AWS\ [m/s]$	$AWA\ [°]$
Beating	*11*	*40*	*5.95*	*16*	*26.2*
Beam	*11*	*90*	*12*	*16.2*	*42.5*
Broad Reach	*11*	*140*	*15.8*	*25*	*116.3*

Table 7: Speeds for different points of sailing

To conduct a thorough analysis, it is necessary to consider the logarithmic wind velocity profile, which, from sea level to the masthead, is not constant. Therefore, given the values of TWS and tangential wind angle TWA measured at the masthead, AWS and AWA undergo a variation in magnitude and direction due to the presence of a logarithmic wind velocity profile $U_w = \frac{u_*}{k}\ln\left(\frac{z+z_0}{z_0}\right)$ (note that $U_w = TWS$ at the masthead). In particular, $k = 0.41$ and $z_0 = 0.1\ m$ are the von Kármán constant (4) and the reference height in free water.
Using the expression of the logarithmic velocity profile, it is possible to evaluate the AWS

vector through Equation 1:

$$U = (U_x)\, e_x + (U_y)\, e_y + (U_z)\, e_z$$

Equation 1: Vector equation of the apparent velocity profile

Where $U_x = TWS\ cos\ (AWA) + U_F$, $U_y = TWS\ sin(AWA)$, and $U_z = 0$ are used for setting the boundary conditions.

The values of AWS and AWA will be used during the setup of the boundary conditions to determine the actual components $(U_x;\ U_y;\ U_z)$.

It is noted that the sail twist has been neglected. To implement this condition in the numerical solver, the profile of the atmospheric boundary layer was derived, given the coordinates of the point at the masthead.

Figure 12, Figure 13, and Figure 14 respectively show the logarithmic velocity profile of the true wind and the apparent wind velocity profile AWS.

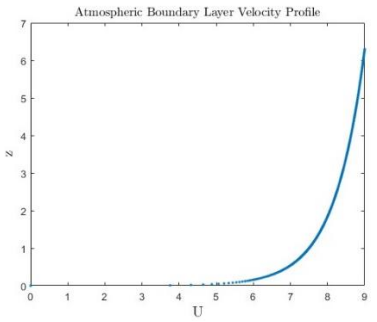

Figure 12: Boundary layer profile and apparent angle as a function of altitude

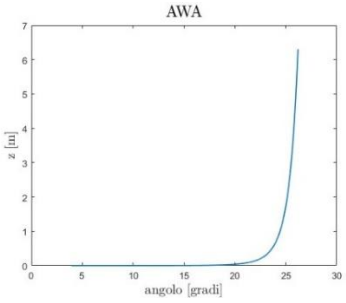

Figure 13: Apparent wind angle as function of altitude

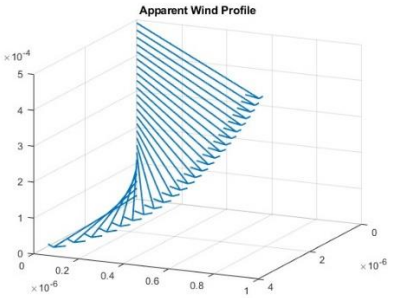

Figure 14: Vector representation of velocity variation with altitude

1.4.2 Study Domain and Grid Construction

The computational domain consists of a parallelepiped inside which the geometry of the object around which the flow is solved is placed. The dimensions of the parallelepiped are appropriately calibrated based on the size of the object around which the flow is solved.

Table 8 shows the dimensions of the block for our case study.

$\boldsymbol{Length\ X\ [m]}$	$\boldsymbol{Width\ Y\ [m]}$	$\boldsymbol{Hight\ Z\ [m]}$
60	*40*	*40*

Table 8: Dimensions of the parallelepiped within which the object exposed to the flow is placed

These dimensions ensure that the faces of the block are sufficiently far from the object so as not to alter its flow, while maintaining a reasonable computational cost.

The parallelepiped was created using the *blockMesh* command, while the surface mesh on the object under consideration was generated using the *snappyHexMesh* command. Furthermore, to achieve a smooth transition between the mesh inside the volume and the surface mesh of the object, a *RefinementBox* was utilized.

Figure 15 and Figure 16 depict the mesh around the vessel.

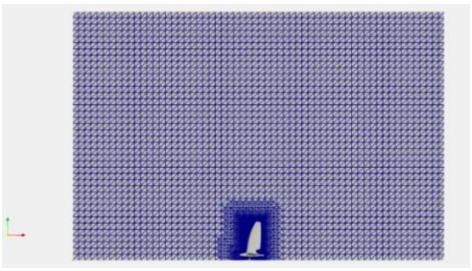

Figure 15: Grid Calculation

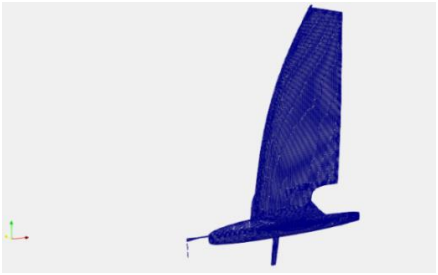

Figure 16: Grid for calculations on the surface of the boat

1.4.3 Simulation Parameter Setup

Regarding the physical properties, the kinematic viscosity of air was set to $\nu = 1.5 \cdot 10^{-5}\ m^2/s$. The vessel was positioned at a height of $0.65\ m$ above the free surface of the water. This value represents an indicative but representative average height observed in flying vessels.
The equations used in the CFD model are the RANS, while the turbulence model employed is the $SST\ k-\omega$, widely used in industrial applications. Additionally, it exhibits good accuracy for case studies with high pressure gradients and separation phenomena.
For the main variables, pressure p and velocity U, Table 9 lists the boundary conditions set in OpenFOAM for the surfaces delimiting the domain.

Surface	***Physical Variables***	***Type***	***Value***
INLET	U	*fixedValue*	Uniform
	p	*zeroGradient*	–
OUTLET	U	*zeroGradient*	Uniform
	p	*fixedValue*	Uniform
FRONT	U	*fixedValue*	Uniform
	p	*zeroGradient*	–
BACK	U	*zeroGradient*	Uniform
	p	*fixedValue*	Uniform
LOWERWALL	U	*fixedValue*	Uniform
	p	*zeroGradient*	–
UPPERWALL	U	*fixedValue*	Uniform
	p	*Slip*	–

Table 9: Boundary conditions for the flow around the boat

Figure 17 shows a representation of the control volume with indications of the faces and the direction of flow inlet.

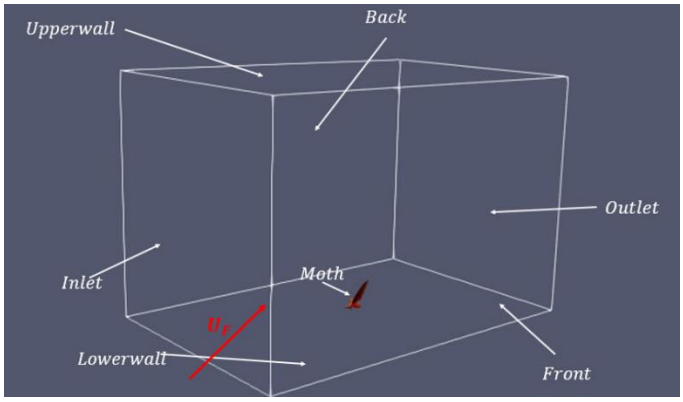

Figure 17: Control volume with indication of the faces and flow direction

The *fixedValue* condition is a Dirichlet condition and imposes a constant value of pressure or velocity. The *zeroGradient* condition is a Neumann condition and imposes a zero pressure/velocity gradient on each cell face. The *slip* condition, instead, represents a sliding condition on the surface (zero normal velocity).

For the cases examined, the incoming flow has a magnitude and direction equal to AWS and AWA. This implies that the incoming flow will be rotated with respect to the boat's reference system by an angle that varies with altitude, as previously described.

For the Beating angle, the flow enters from the *Inlet* and *Front* surfaces and exits from the *Outlet* and *Back* surfaces. For the Reaching angle, the flow enters from the *Front* surface and exits from the *Back* surface. For the Running angle, the flow enters from the Inlet and Front surfaces and exits from the *Outlet* and *Back* surfaces with the boat rotated by 180°. A *slip* condition was imposed on the *upperWall*, while the velocity of the boat U_F was set on the *lowerWall*.

For each analysed case, it was necessary to initialize the values of Turbulent Kinetic Energy (TKE) k $\left[\frac{m^2}{s^2}\right]$ and Specific Dissipation Rate (SDR) ω $\left[\frac{1}{s}\right]$ based on the turbulence intensity I, the flow velocity U_F, and the reference length l. The latter was set equal to the length of the boat itself $l_B = 3.355\ m$.

To solve the governing equations, the steady-state solver simpleFoam was used, referring to the segregated numerical scheme Simple (5).

1.4.4 Sensitivity Analysis with varying grid

The purpose of the sensitivity analysis is to highlight the convergence of the numerical solution as the grid refinement progresses Figure 18 shows the variation of the forces F_x and F_z as a function of the progressive degree of grid refinement. Figure 19 depicts the trend of the residuals, indicating the achievement of a stable solution around 500 iterations.

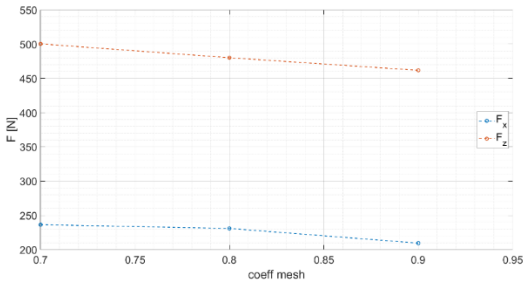

Figure 18: Variation of aerodynamic forces as a function of grid refinement

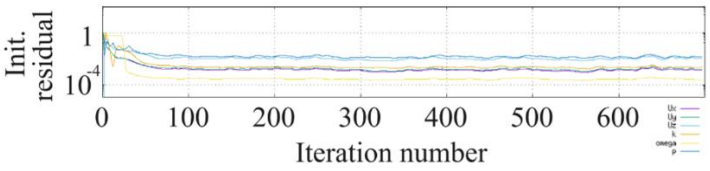

Figure 19: Initial residual trend with iterations

1.4.5 Results Analysis

In this section, the results of the three analysed sailing angles are presented. For each angle, the distribution of static pressure on the hull and the sail is reported, allowing the difference between the windward and leeward sides to be appreciated. Subsequently, streamlines are shown for the leeward side to highlight the vortices generated on the decks and the sail. Finally, the resulting vectors of the forces acting on the decks and the resulting component of the sail responsible for the boat's advancement are reported.

1.4.5.1 Beating Angle

Figure 20-Figure 25 show the pressure distribution and streamlines developed around the vessel for the beating angle.

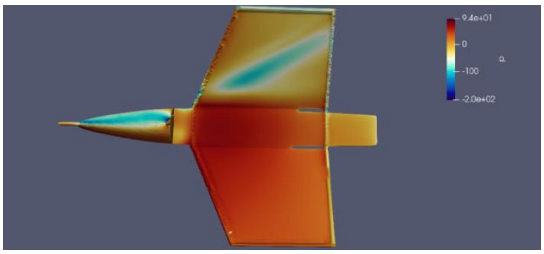

Figure 20: Pressure distribution on the hull - top view

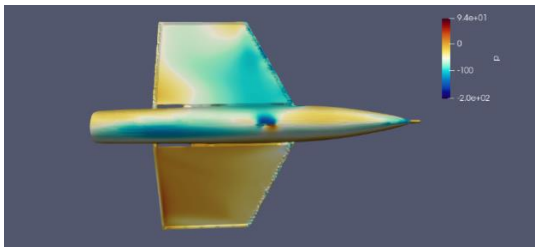

Figure 21: Pressure distribution on the hull - bottom view

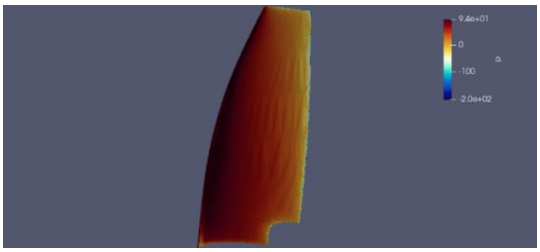

Figure 22: Pressure distribution on the sail - windward side

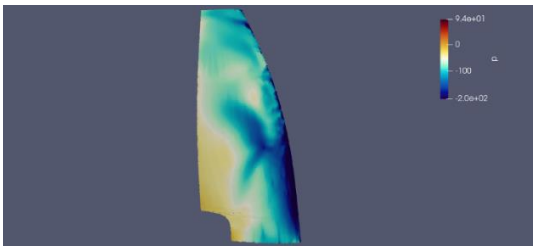

Figure 23: Pressure distribution on the sail - leeward side

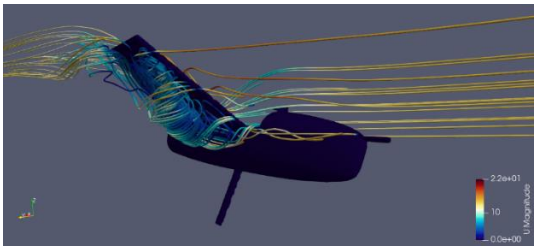

Figure 24: Flow visualization through streamlines over the leeward terrace

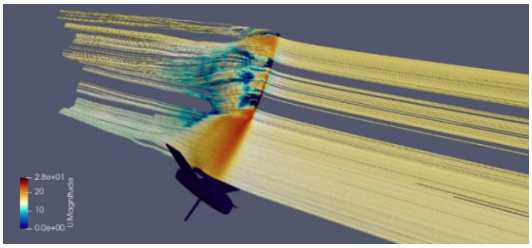

Figure 25: Flow visualization through streamlines over the sail

It is noted that the windward side exhibits high-pressure values due to direct exposure to the asymptotic apparent wind, while on the leeward side, which instead has a non-uniform distribution, lower pressures are localized near the mast, on the lower part. As shown in Figure 22 and Figure 23, pressure non-uniformities on the rear part of the sail are associated with the formation of a recirculation bubble caused by flow separation at the mast. This separation is more intense near the hull, as indicated by the particular shape of the streamlines, which denote a larger recirculation on the lower part. This recirculation can also be observed on the upper part of the decks, which show a low-pressure zone where the flow is separated. On the other deck, the upper part exhibits relatively uniform pressure values, while the lower part shows a situation similar to the leeward sail. This suggests flow separation phenomena also at the decks, which in turn indicate the possible presence of non-negligible pressure forces (and therefore predominantly vertical) that must be taken into account by the Structures department and are analysed quantitatively after briefly describing the other sailing angles.

1.4.5.2 Beam Angle

Figure 26-Figure 31 show the pressure distribution and streamlines developed around the vessel for the Beam angle.

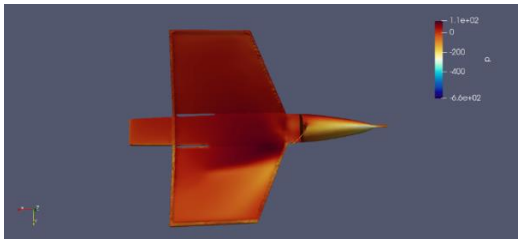

Figure 26: Pressure distribution on the hull - top view

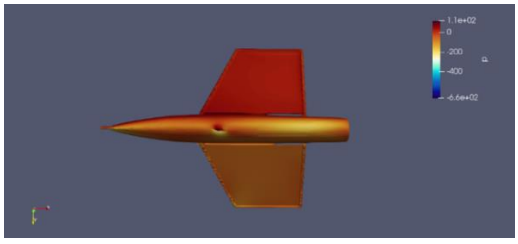

Figure 27: Pressure distribution on the hull - bottom view

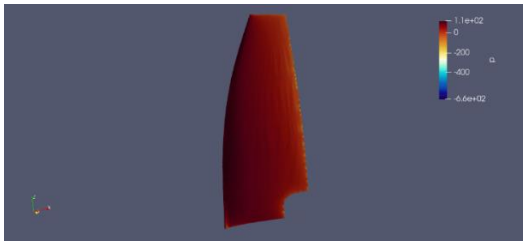

Figure 22: Pressure distribution on the sail - windward side

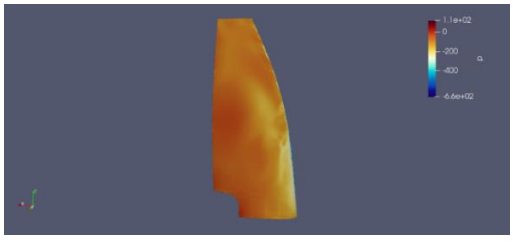

Figure 23: Pressure distribution on the sail - leeward side

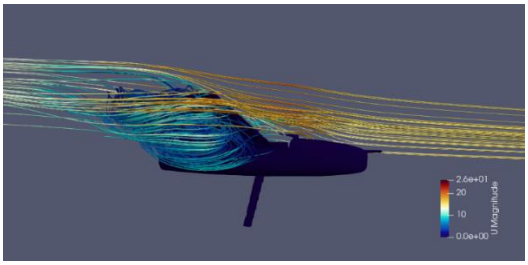

Figure 30: Flow visualization through streamlines over the leeward terrace

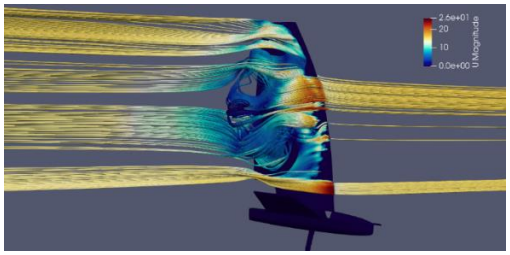

Figure 31: Flow visualization through streamlines over the sail

In this case, flow separation on the sail is much less intense, as shown by the reduced pressure differences between the leeward and windward sides and by the streamlines. Even the decks exhibit more uniform pressure values. On the decks, it is noticeable that differences are appreciable only on one of the two.

1.4.5.3 Broad Reach Angle

Figure 32-Figure 37 show the pressure distribution and streamlines developed around the vessel for the Broad Reach angle.

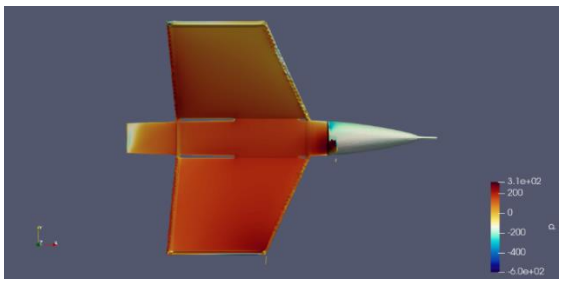

Figure 32: Pressure distribution on the hull - top view

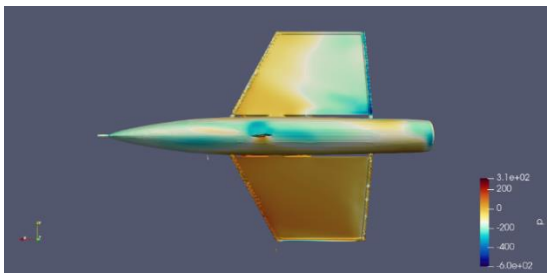

Figure 33: Pressure distribution on the hull - bottom view

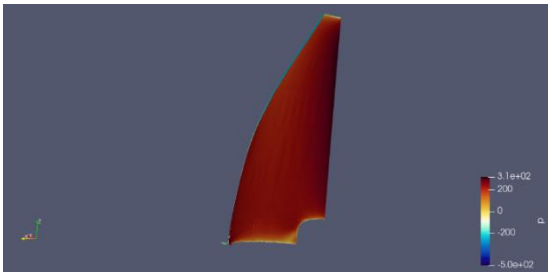

Figure 34: Pressure distribution on the sail - windward side

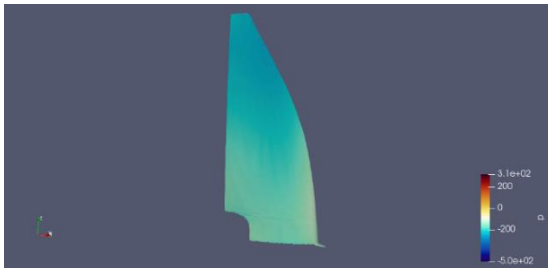

Figure 35: Pressure distribution on the sail - leeward side

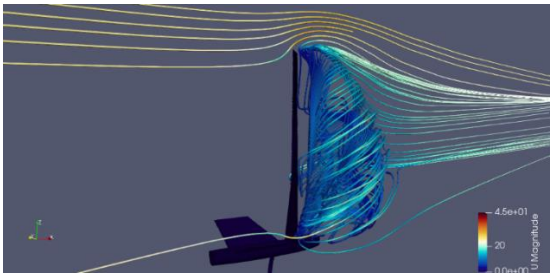

Figure 36: Flow visualization through streamlines over the sail

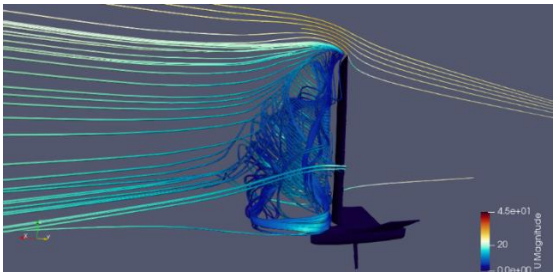

Figure 37: Flow visualization through streamlines over the sail

In this case, the pressure difference between the leeward and windward sides of the sail is significantly greater, as also highlighted by the streamlines. High-pressure differences are also present on the decks. The next section presents the forces resulting from the pressure distributions described in the three cases.

1.4.5.4 Resulting Forces

Figure 38, Figure 39, and Figure 40 depict the loads acting on the decks for the three analysed sailing angles, while Table 10 reports the numerical values.

Figure 38: Vectors of the resultant forces acting on the terraces and on the central part of the hull, for the Beating Angle

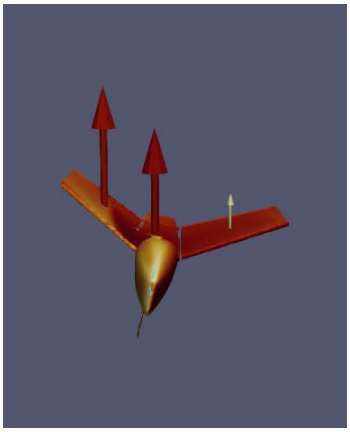

Figure 39: Vectors of the resultant forces acting on the terraces and on the central part of the hull, for the Beam Angle

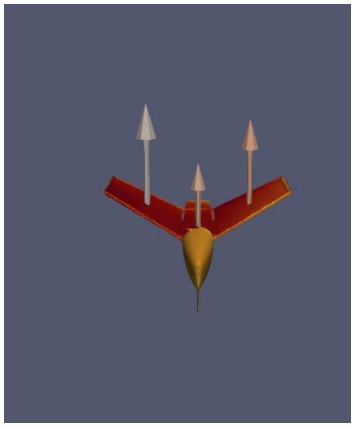

Figure 40: Vectors of the resultant forces acting on the terraces and on the central part of the hull, for the Broad Reach Angle

Vertical Forces $[N]$			
	Beating	***Beam***	***Broad Reach***
Left Wing	*99*	*78*	*224*
Right Wing	*51*	*6.5*	*379*
Hull	*66*	*76.5*	*332*

Table 10: Vertical Forces Wings and Hull

It is noticeable that the running angle by far exhibits the highest loads on the decks, as previously suggested by qualitative flow analyses. Another interesting case is the imbalance of vertical forces between the right and left deck in the reaching angle.
Such quantitative information has been provided to the structures department so that they can take it into account during structural verification analyses and design.

1.5 CFD Analysis of the Main foil and Rudder: Submerged Part

In this section, the aerodynamic performance of the foils used in our vessel is analysed. Figure 41 and Figure 42 show the 3D renderings of the foil and rudder. Note that the foil features a rotatable flap at an angle β of up to approximately 20°.

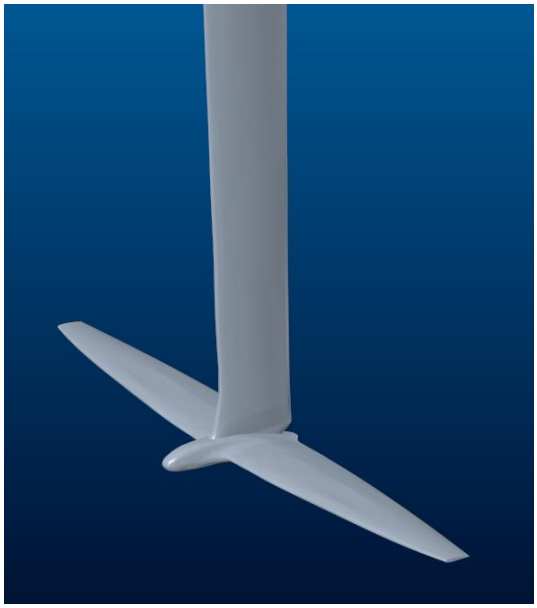

Figure 41: Exocet mainfoil

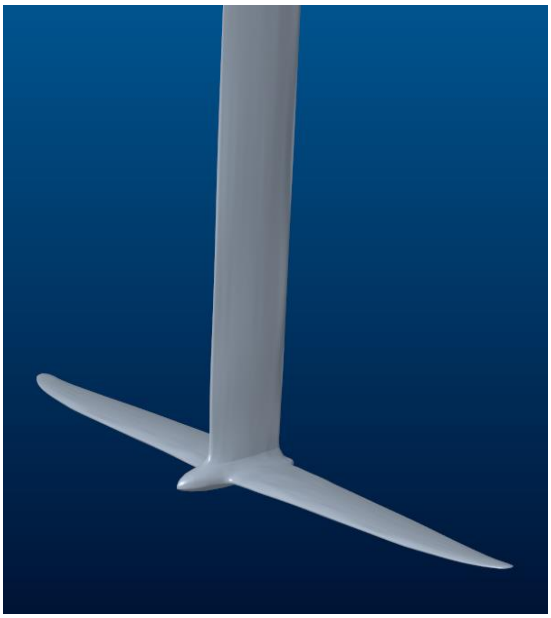

Figure 42: Aardvarkracing Rudder

The main objective is to evaluate the aerodynamic forces exerted by the wing profiles in different configurations, for the same sailing angles analysed in the hull simulations. This allowed us to identify the following information necessary for the structures department:

- the maximum load exerted by the rudder under the most critical conditions, necessary for sizing the Gantry attachments to the hull.
- the maximum horizontal load produced by the main foil, under the most critical conditions, to properly size the bulkhead supporting the keel box.

Simultaneously, following the skipper's indications, the overall contribution generated by the foils was evaluated to ensure:

- Support of the overall weight (skipper + vessel) during different flight phases.
- Lifting of the entire vessel during take-off phase.

1.5.1 Domain and Grid Construction

The dimensions of the parallelepiped constituting the computational grid within which the foils are placed were chosen using the distance $d = 2.355\,m$ between the foils as the reference length.

A block size in the X direction was chosen to be $26\,m$, corresponding to a rear extension of $10d$ and a front extension of $3d$. This ensures fully developed flow at the inlet and allows identification of wake presence at the foil exits.

For the Y direction, we based the block size on the wingspan $b = 1.120\,m$ of the horizontal part of the foil, thus setting the block size in that direction to $12\,m$, approximately $5.5b$ relative

to the longitudinal axis of the control volume.
For the Z direction, with an overall height of the foils $h = 1.350\,m$, a size of $9\,m$ was chosen, corresponding to approximately $6h$.
The preparation of the computational grid was carried out using the same commands as for the hull simulations, based on the same design principles.

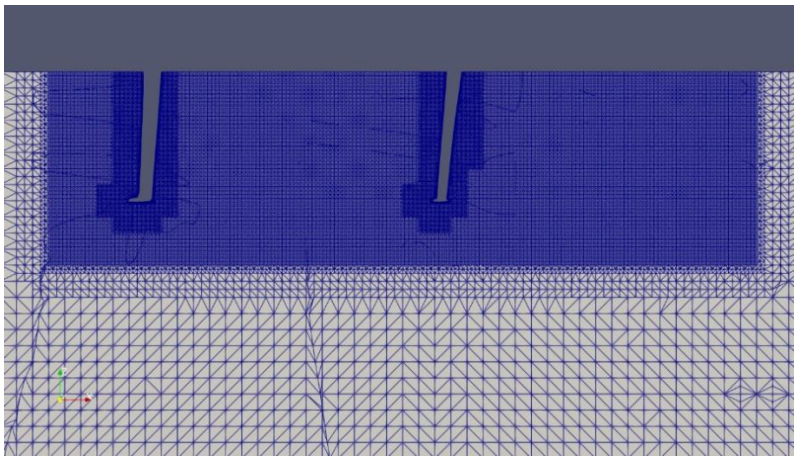

Figure 43: Magnification near the foils of the calculation grid used

As in the case of the hull, it was chosen to implement wall functions, paying attention to discretizing the domain in order to have a $20 < y^+ < 80$. By doing so, the wall functions provide accurate results without the need to discretize the entire boundary layer up to the wall.

1.5.2 Simulation Setup

The simulations were conducted in a water-only phase, therefore it has been set up the kinematic viscosity $\nu = 10^{-6}\,m^2/s$. Furthermore, a draft corresponding to the height used in the hull simulations has been imposed for both the foil and rudder shaft.
The chosen turbulence model is $SST\ k-\omega$, the same as selected for the hull simulations, while the boundary conditions are listed in Table 11.

Surface	***Physical Variables***	***Type***	***Value***
INLET	U	*fixedValue*	Uniform
	p	*zeroGradient*	–
OUTLET	U	*inletOutlet*	Uniform
	p	*fixedValue*	Uniform
FRONT	U	*Slip*	–
	p	*Slip*	–
BACK	U	*Slip*	–
	p	*Slip*	–
LOWERWALL	U	*Slip*	–
	p	*Slip*	–
UPPERWALL	U	*Slip*	–
	p	*Slip*	–

Table 11: Boundary conditions for the flow around the foils

For each sailing angle, the corresponding value of velocity U_F at which the vessel is moving was set.
The analyses were simplified by neglecting the vessel's roll angles. This assumption, at least as a first approximation, is plausible since the two lifting surfaces are at a considerable distance from the surface. Under such conditions, the aerodynamic drag remains unchanged regardless of the roll angle, while the total lift contribution undergoes a rotation around the X-axis (dictated by the foil reference system) equal to the roll angle itself.
This implies that the total lift in the tilted configuration can be manually calculated using simple trigonometric relations. In this case as well, the values of Turbulence Kinetic Energy (TKE) and Specific Dissipation Rate (SDR) were initialized, using a reference length $l = 0.2\,m$ equal to the maximum chord of the horizontal foil.To monitor the convergence of the numerical solution, beyond the residuals set to $1E-12$, the trend of the aerodynamic forces was evaluated as the iterations progressed. For determining the flow field, the *simpleFoam* solver was chosen, in analogy with the flow around the hull and sail.

1.5.3 Sensitivity Analysis

The sensitivity analysis was conducted considering the beating angle, with a flap angle β set to zero. This analysis allows evaluating whether the numerical solution converges as the mesh varies. Since there is no experimental data for comparison, it is necessary to assess the numerical error according to Equation 2 using three meshes, one coarser and the other two progressively finer:

$$\varepsilon_{NUM,i} = S_{n,i} - S_e = C\, h_i^p$$

Equation 2: Numerical Error

The values of the aerodynamic forces obtained from the simulations represent the numerical solutions required for conducting this analysis. To perform such an analysis, it's necessary to eliminate the iterative error from the numerical solution. Figure 38 shows the trend of the aerodynamic forces for the beating angle with $v = 5.95\,m/s$ as the mesh varies. In Figure 39, instead, the trend of the convergence order $\tilde{P}$ for lift and drag forces is shown. Their relationship is described in Equation 3:

$$\tilde{P} = \frac{\log\left(\frac{S_{n,1} - S_{n,2}}{S_{n,2} - S_{n,3}}\right)}{\log\left(\frac{h_2}{h_3}\right)} - \frac{\log\left(\frac{\left(\frac{h_1}{h_2}\right)^p - 1}{\left(\frac{h_2}{h_3}\right)^p - 1}\right)}{\log\left(\frac{h_2}{h_3}\right)}$$

Equation 3: Order of convergence evaluation

While the ratios between the heights $\frac{h_1}{h_2}$ and $\frac{h_2}{h_3}$ were evaluated according to the relationship $\frac{h_i}{h_j} = \sqrt[3]{\frac{N_j}{N_i}}$, while $S_{n,1}$, $S_{n,2}$ and $S_{n,3}$ are the numerical solutions.

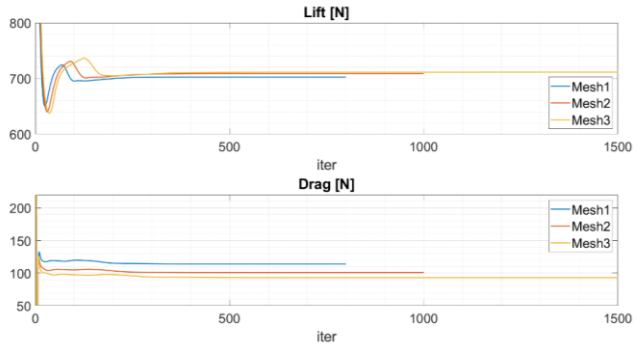

Figure 44: Convergence of lift and drag values with the number of iterations, for the three considered meshes

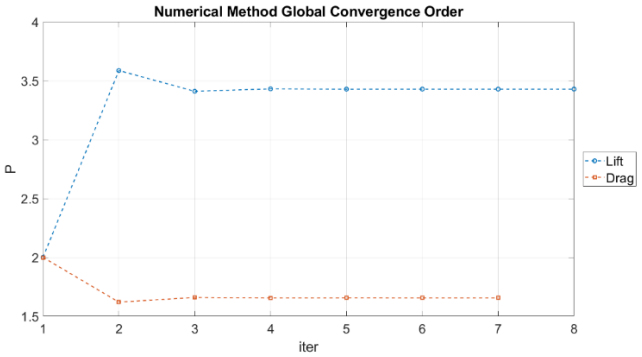

Figure 45: Convergence order as a function of iterations

Once the convergence order was determined and the result deemed acceptable, the remaining analyses were conducted using the intermediate mesh as it represents the best compromise between accuracy and computation time.

1.5.4 Results Analysis

1.5.4.1 Flight Phases

The three main sailing angles were analysed: Beating, Beam, and Broad Reach, in which the flap angle of the horizontal part of the main foil β was set to 0°.

Setting conditions $\beta = 0$ [°]		
	F_L $[N]$	F_D $[N]$
***Beating*: $v = 5.95$ $[m/s]$**	*708.81*	*100.90*
***Beam*: $v = 12$ $[m/s]$**	*2919.37*	*380.29*
***Broad Reach*: $v = 15.8$ $[m/s]$**	*5081.43*	*642.19*

Table 12: Aerodynamical Forces

For the Broad Reach configuration, two visualizations are provided. Specifically, Figure 46 shows the pressure distribution and streamlines, while Figure 47 displays the velocity distribution at the symmetry plane.

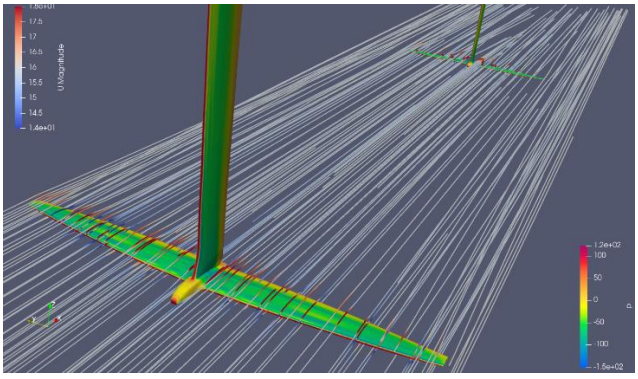

Figure 46: Pressure distribution on surfaces and streamlines - Broad Reach

Figure 47: Colour map of the velocity magnitude on the symmetry plane - Broad Reach

Next, only the main foil with $\beta = 0°$ was analyzed to assess the force distribution considering

the overall contribution. Again, all three sailing angles were analyzed. Figure 48 and Table 13 show the results for Lift, while Figure 49 and Table 14 present the results for Drag.

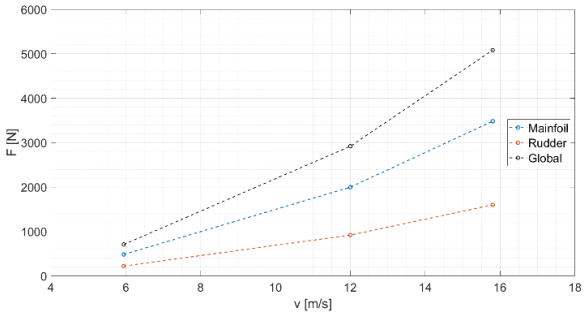

Figure 48: Lift contributions of the main foil and rudder as a function of velocity (i.e., sailing condition)

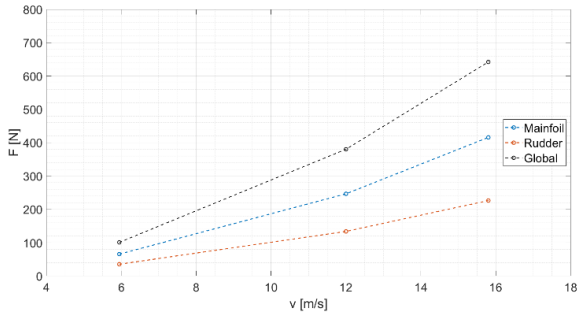

Figure 49: Drag contributions of the main foil and rudder as a function of velocity (i.e., sailing condition)

Global Lift		
	$\boldsymbol{Main}\ [\boldsymbol{N}]$	$\boldsymbol{Rudder}\ [\boldsymbol{N}]$
Beating: $v = 5.95\ [m/s]$	484.76	224.05
Beam: $v = 12\ [m/s]$	1999.33	920.04
Broad Reach: $v = 15.8\ [m/s]$	3481.54	1599.89
$\boldsymbol{\Delta Lift}\ [\%]$	68	32

Table 13: Lift contributions of the main foil and rudder as the speed (i.e., sailing condition) varies

Global Drag		
	$\boldsymbol{Main}\ [\boldsymbol{N}]$	$\boldsymbol{Rudder}\ [\boldsymbol{N}]$
Beating: $v = 5.95\ [m/s]$	65.61	35.29
Beam: $v = 12\ [m/s]$	241.57	133.72
Broad Reach: $v = 15.8\ [m/s]$	415.86	226.32
$\boldsymbol{\Delta Drag}\ [\%]$	65	35

Table 14: Drag contributions of the main foil and rudder as the speed (i.e., sailing condition) varies

The highest lift (and also drag) forces are once again determined in the Running condition, characterized by the highest velocity value. The distribution of lift and drag between the rudder and main foil remains unchanged for all three sailing angles. Furthermore, the worst-case scenario occurs in Upwind, where the aerodynamic forces are significantly lower than the weight of the boat. To address this, it is well-known that it's possible to adjust the flap angle of the main foil to increase the lift contribution, as described in the following section.

1.5.4.2 Effect of Flap Angle

Subsequently, the analysis focused on studying the effect of the flap angle to ensure take-off at low speeds.

The chosen wind condition was extrapolated from the polar diagram, corresponding to an Upwind angle and $TWS = 5\ m/s$, for which a boat speed of $U_F = 4\ \mathrm{m/s}$ is identified.

Figure 50,Figure 51, Figure 52 show the three flap angles of the horizontal part of the main foil.

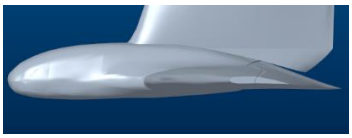

Figure 50: 5° - flap

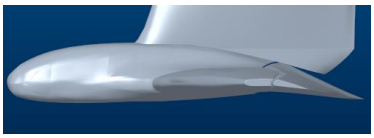

Figure 51: 10° - flap

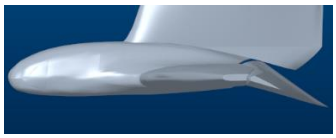

Figure 52: 20° - flap

Table 15 shows the aerodynamic forces varying with the flap angle for the configuration involving both foils.

Setting conditions – $\boldsymbol{Beating}$, $\boldsymbol{TWS} = 5\ [\boldsymbol{m/s}]$		
Flap – Angle [°]	$\boldsymbol{F_L}\ [\boldsymbol{N}]$	$\boldsymbol{F_D}\ [\boldsymbol{N}]$
5	*552.1*	*69.89*
10	*711.1*	*87.22*
20	*943.2*	*150.76*

Table 15: Lift and drag contributions of the main foil and rudder as the flap angle varies

Figure 53 and Table 16 present the results for lift, while Figure 54 and Table 17 depict the results for drag, both as functions of the flap angle.

Global Lift				
Flap – Angle [°]	$\boldsymbol{Mainfoil}\ [\boldsymbol{N}]$	$\boldsymbol{Rudder}\ [\boldsymbol{N}]$	$\boldsymbol{\Delta Lift}\ [\%] - \boldsymbol{Main}$	$\boldsymbol{\Delta Lift}\ [\%] - \boldsymbol{Rudder}$
5	*441.8*	*80.25*	*84.63*	*15.37*
10	*624.4*	*86.65*	*87.81*	*12.19*
20	*870*	*73.20*	*92.24*	*7.76*

Table 16: Lift contributions of the main foil and rudder as the flap angle varies

Global Drag				
Flap – Angle [°]	$\boldsymbol{Mainfoil}\ [\boldsymbol{N}]$	$\boldsymbol{Rudder}\ [\boldsymbol{N}]$	$\boldsymbol{\Delta Drag}\ [\%] - \boldsymbol{Main}$	$\boldsymbol{\Delta Drag}\ [\%] - \boldsymbol{Rudder}$
5	*50.60*	*19.29*	*72.40*	*27.60*
10	*68.71*	*18.51*	*78.78*	*21.22*
20	*115.51*	*35.25*	*76.62*	*23.38*

Table 17: Drag contributions of the main foil and rudder as the flap angle varies

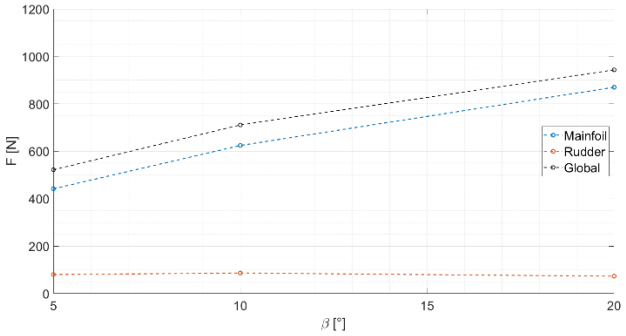

Figure 53: Lift contributions of the main foil and rudder as the flap angle varies

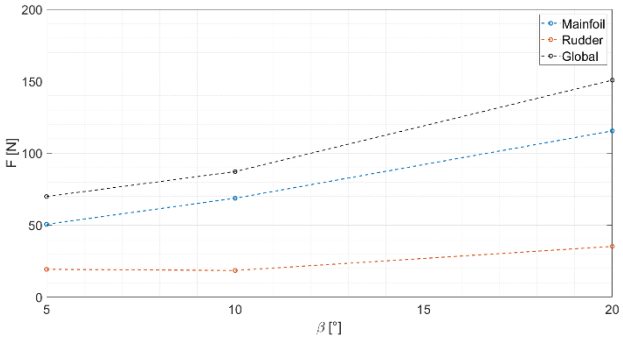

Figure 54: Drag contributions of the main foil and rudder as the flap angle varies

Below are the velocity distributions at the symmetry plane for the three aforementioned flap angles.

Figure 55: Colour map of the velocity magnitude on the symmetry plane – 5° flap

Figure 56: Colour map of the velocity magnitude on the symmetry plane – 10° flap

Figure 57: Colour map of the velocity magnitude on the symmetry plane – 20° flap

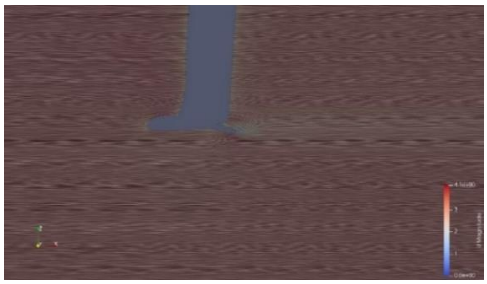

Figure 58: Line Integral Contours – 20° flap

The purpose of this analysis is to compare, at the same sailing angle, the lift and drag forces. Referring to Table 12 and Table 15, it is noted that the total lift force is equated by setting a flap angle of around $10°$, resulting in lower aerodynamic drag (due to a velocity setting of $v = 4\,m/s$).

The lift contribution of the main foil becomes more pronounced as the flap angle increases; conversely, the lift contribution of the rudder decreases. The aerodynamic wakes for configurations with flap angles of $5°$ and $10°$ is nearly identical, although a greater inclination of the wake can be observed for a flap angle of $10°$. This is reflected in the numerical results, which show a 6% reduction in drag contribution.

In contrast to the first two configurations, it is observed that the wake for the configuration with a $20°$ flap angle has a greater height and fully encompasses the rudder. This results in a percentage increase in rudder drag and a slight reduction in mainfoil drag compared to the configuration with $\beta = 10°$.

These considerations are associated with the presence of a large separation zone in the rear part of the main foil, where flow stall can be observed (see Figure 58).

1.5.4.3 Calculation of Take-off Speed

For the calculation of the take-off speed, the roll angles corresponding to each sailing angle and the $C_{L,max}$ values were used, adimensionalizing the previously calculated forces (Table 18).

	Roll Angle [°]		***Flap Angle*** [°]	$C_{L,max}$
Beating	*25*		*5*	*0.49*
Beam	*12.5*		*10*	*0.67*
Broad Reach	*0*		*20*	*0.89*

Table 18: Values of the roll angle and lift coefficient

Therefore, Table 19 reports the take-off speed $U_{dec} = \left(\frac{2\,W}{\rho\,S\,C_L}\right)^{\frac{1}{2}}$ evaluated as a function of the roll angle and $C_{L,max}$, which depends on the respective flap angle.

$\boldsymbol{Flap\ Angle}$ [°]	$\boldsymbol{U_{dec}\ [m/s] - Beating}$	$\boldsymbol{U_{dec}\ [m/s] - Beam}$	$\boldsymbol{U_{dec}\ [m/s] - Broad\ Reach}$
5	*6.63*	*6.38*	*6.31*
10	*5.68*	*5.47*	*5.40*
20	*4.93*	*4.75*	*4.69*

Table 19: Take-off speed as a function of flap angle and sailing condition

For the beam reach and broad reach, we observe a take-off speed significantly lower than the cruising speed for these headings (see Table 7). Therefore, the most critical condition is close-hauled. Indeed, for this heading, the reference speed is $5.95\ m/s$, thus takeoff can only occur with a flap angle of at least approximately $10°$.

1.6 Wings and Rig

The design of the Moth's wings must consider the sustainability of materials, and the structural and operational needs. A careful selection of materials is crucial to ensure the production of efficient, safe, environmentally friendly wings that meet the required performance criteria, such as strength, rigidity, and durability. It is essential that the selected materials can be easily processed and assembled using available techniques and tools without compromising quality or structural integrity. Therefore, our design emphasizes the importance of an integrated approach that considers all these factors, thus contributing to promote more sustainable practices in the maritime sector.

The preliminary phase of the design primarily focused on structural analysis, aimed at developing computational models to evaluate the strength and serviceability performances of the wings modelled as cantilever beams. The analyzed loading condition takes into account the load generated by the skipper's weight and its dynamic effects, the load produced by the lateral rigging supporting the mast, and a combination of these two loads. The tubular cross-section was determined iteratively, assuming it to be made of homogeneous material, and to ensure a versatile design, various materials such as carbon fiber, aluminum, and flax fiber were considered. Initially, a thorough comparison was made between the deformations and stresses obtained from the analyses by adopting uniform diameters among the different materials, as this approach allows for the identification of the general trend of the mechanical performance of the various materials.

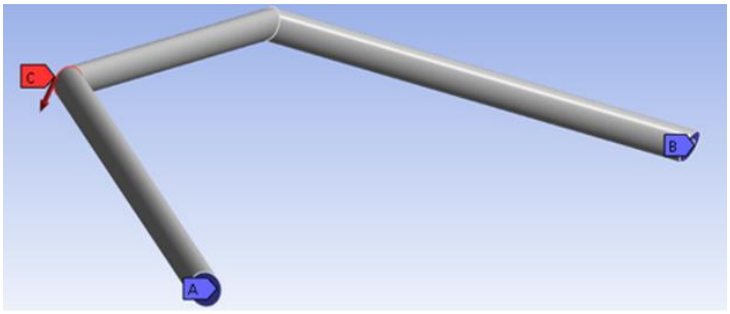

Figure 59: Wings with tubular frame

In the second phase of the design, the wings have been represented by a FEM model using BEAMS elements in *ANSYS®* environment. The stiffness and inertia properties of the beam are represented by a cross-section, which can vary along the length of the beam itself, thus requiring the definition of geometric and mechanical properties, as well as the arrangement and connection of nodes to define the structure's topology.

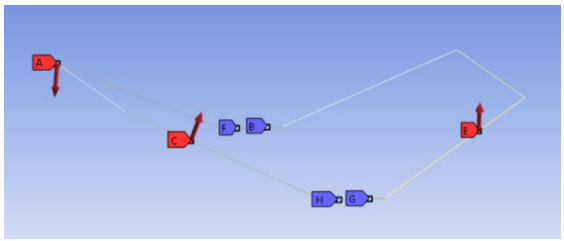

Figure 60: Load configuration

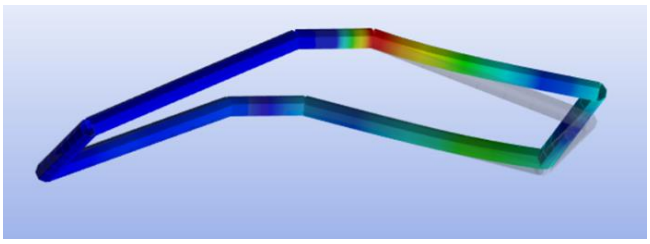

Figure 61: Stress distribution and deformed state

A specific analysis was conducted for each type of material, evaluating the strength and deformability to determine the optimal cross-sectional shape that complied with the imposed limits. However, the critical limit state was the flexural buckling strength, given the slenderness of the chosen structural elements. The cross-section, resulting from the specific analyses, was defined for two solutions considering carbon fiber (6) and aluminum, as reported in (Table 14). The mechanical properties of aluminum are reported according to UNI 8278.

CROSS-SECTION OF WINGS				
MATERIAL	$Outer\ Diameter$ $[mm]$	$Thickness$ $[mm]$	$Tensile\ Modulus$ $[GPa]$	$Tensile\ Strenght$ $[MPa]$
Carbon Fiber Biax	*50*	*2*	*68,9*	*4120*
Aluminum 6061-T6	*60*	*2*	*234*	*305*

Table 14: Cross-section and materials of wings

The material choice was made through careful analysis, considering various key factors such as the workability of the material, its availability on the market, and, most importantly, the overall weight of the wings.

In the case of carbon fiber, a significant reduction in overall weight was highlighted, thanks to its lower density compared to aluminum 6061. Carbon fiber indeed has a density of about 1800 kg/m^3, while aluminum 6061 has a density of about 2700 kg/m^3. This notable weight advantage positively influenced the material choice, considering the importance of lightweight in this sector.

However, it is important to emphasize that aluminum 6061 was considered a hypothetical alternative for several reasons. This material, besides being lightweight, exhibits sufficient strength to withstand stresses and notable corrosion resistance. Additionally, the T6 treatment enhances its mechanical properties, particularly strength and hardness, offering an optimal balance between strength and ductility.

However, the adoption of carbon fiber offered us the opportunity to reuse damaged Standard Diameter Mast (SDM) windsurfing masts that would otherwise have been discarded. These masts are characterized by greater stiffness compared to Reduced

Diameter Mast (RDM) models and larger diameters.
The fastening and anchoring of the wings to the hull plays a crucial role in the overall design of the boat. The main objective is to ensure that the wings are securely and robustly connected to the hull, so they can withstand the stresses generated during its service.
The critical points are represented by the locations of the bolted connections between the wings and the hull (see Figure 62, Figure 63, Figure 64, and Figure 65). A steel plate was designed and installed at each of the critical points. In Table 20, the values of reaction at critical points are reported, derived from the specific loading condition outlined earlier.

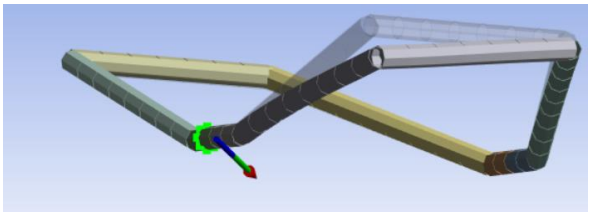

Figure 62: First force reaction

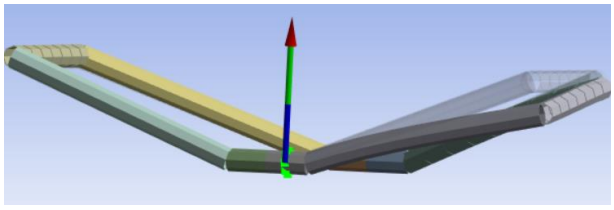

Figure 63: Second force reaction

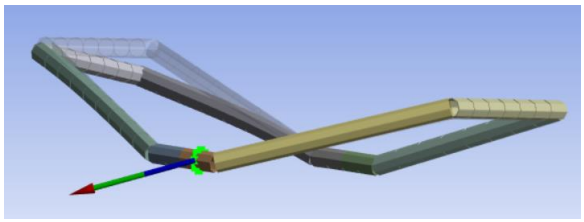

Figure 64: Third force reaction

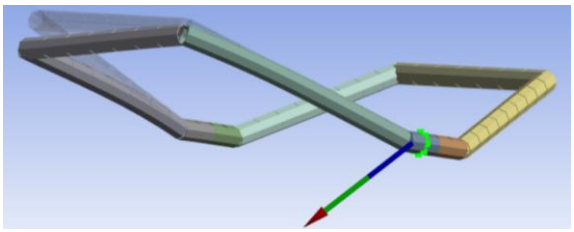

Figure 65: Fourth force reaction

Reaction [N]	1	2	3	4
F_x	-50,67	230,71	-924,27	-624,25
F_y	-43,99	84,85	1644,50	549,86
F_z	-11,52	1784,80	-768,26	-786,98
F	68,09	1801,70	2036,90	1145,20

Table 20: Reaction forces

Stainless steel was chosen as the material for the plates due to its mechanical performance and excellent corrosion resistance properties, ensuring durability even in marine environments.
The plates underwent careful analysis to assess the tensile stresses and deformations they may be subjected to during use, to understand their structural behaviour. Another critical point is represented by the anchoring to the lower bulkheads. A ductile joint system was developed to address this criticality, which involves the use of appropriately sized screws and bolts.

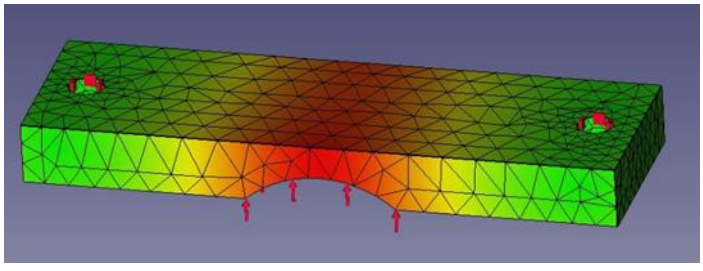

Figure 66: Steel plate

CHARACTERISTICS OF STEEL PLATE				
$Width\ [mm]$	$Lenght\ [mm]$	$Thickness\ [mm]$	$BOLT\ CLASS$	$Stress\ [MPa]$
30	160	6	M6	195

Table 15: Characteristics of steel plate

1.7 Keelbox

The design process of the keel box began with a careful evaluation of the shape of the existing mold. This component plays a crucial role, not only housing the keel as it passes through the hull but also retaining it, especially in the upper part, and is therefore subjected to significant stresses. During the design of the keel box, it was necessary to adapt the shape of the existing mold to accommodate the wings designed by our team. This required the creation of a wooden filler core to fill the voids present in the original wings of the mold. At the same time, it was necessary to modify the geometric dimensions of the keel box to allow the wings to protrude and the installation of the controls that will be connected to the wand. Therefore, the height of the keel box was increased to meet these specific requirements.

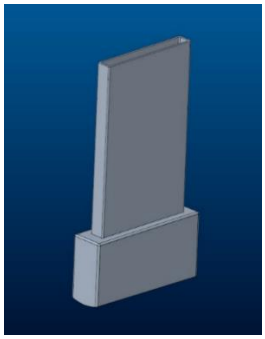

Figure 67: Keel box

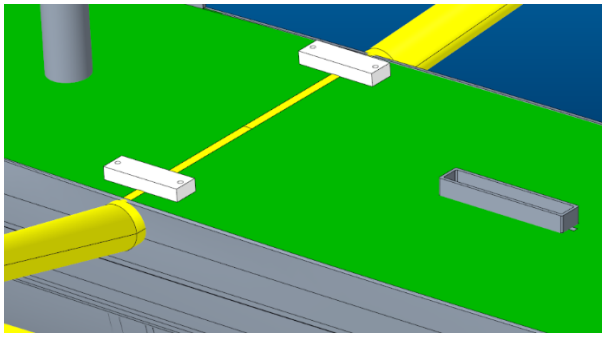

Figure 68: An overall overview of the keelbox protrusion for the attachment of wand controls

The 3D modeling and printing department was responsible for translating the design requirements into a specially modelled and printed keel box in PETG. PETG was chosen as the material for its mechanical and thermal resistance, as well as its flexibility and resistance to atmospheric agents. Compared to PLA, PETG offers greater heat resistance and flexibility, making it ideal for applications subjected to mechanical stress.
Furthermore, excellent layer adhesion allows us to produce prints with reliable water tightness, which is essential for marine applications. These characteristics make PETG an ideal choice to produce the keel box, ensuring the durability and performance required in the marine environment.

1.8 Electronics and data acquisition

As a new team our goal is to get all the possible data from our first experience to improve by year in year.
Our sensors team set his goal to produce the information from the boat to be entrusted to other departments through different projects.
The planned objectives concerned the monitoring of the following parameters:

1) Pitch, Roll and Yaw
2) Height of flight
3) Loads on the ropes
4) Position
5) Expected speed

1) To measure the value of the Pitch, Rall e Yaw we choose to use a "Gravity: 10 DOF IMU AHRS BNO055 + BMP280" provided by our sponsor DFRobot.
The BNO055 module is an integrated circuit to implement a 9-axis IMU. It includes a 14-bit triaxial accelerometer, a 16-bit triaxial gyroscope, a triaxial geomagnetic sensor, and a 32-bit microcontroller. It is extremely compact and can provide individual data of the three types of sensors and integrated data such as quaternions, Euler angles or vectors.
The BMP280 module is an absolute barometric pressure sensor.
It measures barometric pressure and temperature, convertible into altitude by a specific formula. Based on Bosch piezoresistive pressure sensor technology, it offers high precision, linearity, long-term stability and EMC robustness. The two modules "BNO055" and "BMP280" are integrated on a single board, combining the two sensors in a 10 degree of freedom module. The standard Gravity-I2C interface simplifies the integration process.
2) To keep track of the flight height we opted for two ultrasonic sensors "A02YYUW" also provided by our sponsor DFRobotic.
The function of this sensor is outlined by the following points:

- Pulse Transmission: The sensor emits high frequency sound pulses.
- Reception of reflections: The sound impulses propagate in space and hit the surrounding objects. When a pulse hits an object, it is reflected back towards the sensor.
- Flight time measurement: The sensor measures the time taken by the sound pulses to travel to the object and back. This flight time is proportional to the distance between the sensor and the object.
- Distance calculation: Using the measured flight time and sound speed, the sensor calculates the distance between itself and the object.

3) To track the load in the ropes we decide to use a "Smart**link**^{2} Nano" by Cyclops Marine which will transduce the load tension and send it via Bluetooth to our core which will process the data of all the sensors.
Our goal is to create a live telemetry to be provided to our skipper and that can be displayed.
4) Tracking the position is one of the most important objectives as the idea is to merge it with all the other sensors in order to understand what happens, where, and in what state the boat is at that particular moment. The GPS we decided to use is the "Garmin 18x LVC" that detects signals transmitted by GPS satellites using a high-sensitivity antenna and based on signals received from different satellites, it calculates its position using the trilateration method. To be able to send the data to our core we decided to always opt for Bluetooth technology by connecting it, thanks to appropriate measures to a "ESP32-S2-DevKitM-1" also provided by our sponsor DFRobots.
5) The last project, this time software, that we decided to implement is a "VPP" or a "Velocity Prediction Program" to 6 degrees of freedom that can provide an estimate of the speed and

an analysis of the performance of our boat even before putting it in the water.
Because of the amount of work it is still under development, but we are confident to complete it by the end of 2024.

2 MANUFACTURING AND COST ANALYSIS

2.1 General description

This paragraph is intended to provide a general overview of the construction phase of the fundamental and crucial elements.

2.2 Hull

The mold, kindly provided by a private company as a gift, unfortunately, did not meet our design requirements, making significant changes necessary to adapt it to our needs. The main problem was the incompatibility of the wings shape with the mould. After a careful analysis of the available options, we decided to adapt the mould using handmade fir wood slabs. This solution has allowed us to maintain the structural integrity of the mould, making it suitable for our rolling needs. The wooden slabs were fixed on the mould using hot melt glue, ensuring a secure seal during the lamination process. To ensure an optimal result, before the infusion, we paid special attention to the accurate positioning of the skins and core on the adapted mould. In addition, to achieve a perfect and hassle-free vacuum, the remaining gaps after installing the insoles were filled with foam. This has helped to maintain a uniform surface during the rolling process, ensuring a quality end result. During the rolling process, a problem arose in the part of the bow attributable to the mould itself, which necessitated corrective action. We then decided to recreate the damaged part and then glue it to the hull. To meet this challenge, the mold has undergone a thorough repair and preparation process. It was sanded to eliminate imperfections; a layer of gel coat was applied to improve the quality of the surface and the porous points were covered with bundle tape to ensure a flawless lamination. Thanks to these targeted interventions and our attention to detail, the bow-rolling process has been successfully completed. The damaged part was repaired successfully, and the end result lived up to our expectations of quality and precision.

Figure 69: Modification of the mould with the wooden slabs after infusion

HULL materials				
Piece	**Unit**	**Quantity**	**Unit Cost**	**SubTotal Cost SM$**
Flax Twill 200g	kg	0,82	0,00	0,00
Flax Twill 200g Saddles	kg	0,76	0,00	0,00
Flax Biax 350g	kg	3,23	0,00	0,00
Poweribs	kg	0,97	0,00	0,00
Poweribs saddles	kg	0,16	0,00	0,00
PET Core 5mm	kg	2,63	20,00	52,60
Kevlar twill 300g	kg	0,18	120,00	21,00
Carbon biax 210g	kg	0,01	200,00	2,10
Spabond (hull and saddles)	kg	2,00	25,00	50,00
Epoxy IB2 Infusion	kg	9,36	15,00	140,40
Epoxy STD lamination	kg	5,95	25,00	148,84
Carbon sleeve	kg	0,01	200,00	201,60
Vacuum Bag	sqm	5,00	2,00	10,00
Peel Ply	sqm	5,00	5,00	25,00
Mesh	sqm	5,00	1,90	9,50
Perforated Plastic	sqm	5,00	0,90	4,50
Vacuum Hose 6mm	lm	15,00	1,00	15,00
Spiral Tube	lm	10,00	1,00	10,00
Tacky Tape	15m roll	2,00	8,00	16,00
Release Agent	liter	0,50	100,00	50,00
TOTAL				**556,54**

Table 21: Cost Analysis of hull materials

2.3 Foils, Rig and Components

The Table 22 shows the components that have been purchased along with their respective costs.

FOILS, Rig and Components				
Piece	**Unit**	**Quantity**	**Unit Cost**	**SubTotal Cost SM$**
Main Foil	pcs	1		2000
Rudder	pcs	1		2000
Mast	pcs	1		0
Boom	pcs	1		0

Spreader	pcs	1		0
Gantry	pcs	1		0
Gantry-Hull Carbon tube	pcs	1		0
Control Lines	\	\	\	500
Blocks	\	\	\	2700
Recycled Polyester Sail	pcs	1		0
TOTAL				**7200**

Table 22: Analysis of the cost to the purchased components

2.4 Wings

For the wings, although the mold provided presented a rigid design, we made the decision to make tubular wings. Initially, we considered using aluminum as a material, but after having had the opportunity to give a second life to the carbon windsurfing trees that were donated to us, we opted for the construction of the wings in such a way. These pieces were machined to fit the desired design, reconstructing the measurements and angles required for assembly. After cutting the carbon tubes, with the correct angles and lengths, we are proceeding with the assembly using a glue (spabond) that ensures perfect stability between the two pieces. To make it even safer to break it is thought to use later a carbon sock in the most stressed corners, respecting the percentage of 5% of carbon usage dictated by the regulation.

Figure 70: Bonding of wings

Wingbars				
Piece	**Unit**	**Quantity**	**Unit Cost**	**SubTotal Cost SM$**
Carbon Sleeve	kg	0,15	200,00	29,52
Upcycled Windsurf Masts	kg	4,05	0	0
Spabond	kg	0,40	25,00	10,00
Epoxy STD lamination	kg	0,21	25,00	5,17
TOTAL				**45**

Table 23: Analysis of the cost to the employed wingbars materials

2.5 3D Printing

3D Printing & Reinforcements				
Piece	**Unit**	**Quantity**	**Unit Cost**	**SubTotal Cost SM$**
Keelbox	kg	0,70	15,00	10,50
Hull L-shaped attachments	kg	0,20	15,00	3,00
Wingbars fittings	kg	0,24	15,00	3,60
Stern wingbars fitting	kg	0,15	16,00	2,40
Wingbars fittings	h	10,00	20,00	200,00
Keelbox printing	h	15,00	20,00	300,00
Hull L-shaped attachments	h	11,00	20,00	220,00
Stern wingbars fitting	h	7,00	20,00	140,00
Glass Fiber Twill 300g	kg	0,05	75,00	4,05
Epoxy STD lamination	kg	0,05	25,00	1,35
TOTAL				**884,90**

Table 24: Analysis of the cost to the printed components and reinforcement

2.6 Materials

All materials used shall be discussed briefly from an engineering point of view (Sustainability will be addressed on Section 3).

General Consumables				
Piece	**Unit**	**Quantity**	**Unit Cost**	**SubTotal Cost SM$**
Vacuum bag for hull reinforcements	sqm	5.00	2.00	10.00
Brushes	pcs	12	2	24.00
breather	sqm	2.6	3	8
Polyester Filler (gelcoat-like)	kg	0.66	15	10
Vacuum hose 6mm	lm	15.00	1.00	15
Mesh	sqm	2.00	5.00	10
PeelPly	sqm	2.00	1.90	4
Fusion Fix Spray Glue	kg	1	50	50
Masking Tape	Roll	5	2.99	15
Gloves	100 pack	3	3.99	12
Tacky Tape	15m roll	5.00	8.00	40.00
Okume (bulkheads)	kg	3.8	0	0
Poplar (bulkheads and hull mould fittings)	kg	4.2	0	0
Steel	kg	0.3	15	4.5
TOTAL				**202**

Table 25: Analysis of the cost to the general consumables

2.7 All other elements

SM$ Total Balance	
Hull Materials	556,54
Foils, Rig and Components	7200
3D Printing & Reinforcements	884,90
General Consumables	202

	Wingbars	45
	TOTAL	**8888,00**

By analysing all the tables and summing up the costs for each working phase, it emerged that the budget of 10,000 Sumoth dollars was respected.

3 SUSTAINABILITY ANALYSIS

3.1 General description

During our participation in the SuMoth Challenge, we encountered several obstacles in our boat's design and production process. Time constraints compelled us to focus our production primarily on the hull. The hull, derived from a second-hand mold sourced from a freelance boat builder, allowed us to give a second life to material otherwise destined for landfill. To fully understand the environmental impact of our boat, we conducted a detailed analysis of the components and processes involved in its creation. This enabled us to identify the key components contributing to the overall impact. We opted for materials with a lower ecological footprint, such as flax fiber over carbon fiber, and utilized Okume wood and Bioresins.

3.2 Boat and elements lifecycle

Sustainability has become a crucial aspect in the design and production of racing boats. One of the main highlighted points is the upcycling of components from old vessels. This practice not only reduces the environmental impact resulting from the production of new materials but also contributes to waste reduction. Despite challenges related to time constraints, particular attention has been paid to reduce the environmental impact and ecological footprint during boat production. Attention to the selection of appropriate materials and controlling production processes has helped reduce the overall environmental impact of production. However, opportunities have been identified to further enhance and refine production practices to reduce the use of polluting materials and improve the overall lifecycle of the boat. The future use of the boat after the competition has influenced decisions regarding the final treatment of components. Various options have been examined for the final treatment of boat components at the end of their lifecycle. Recycling techniques have emerged as a key strategy, particularly for composite materials, which can be challenging to dispose of sustainably.

3.3 Hull

To fully understand the recycling process, it is essential to comprehend the composition of the hull itself. In its construction, composite materials are used to optimize performance, durability, and lightweight properties. The composite material for boat hulls often consists of alternating reinforcing fibers and resin layers. In this case, flax fiber is used as the reinforcement material, while bio-resin is the matrix that binds the fibers together. The assembly of these composite materials occurs through lamination and polymerization processes, creating a lightweight yet sturdy hull. However, when a hull reaches the end of

its useful life or undergoes irreparable damage, it becomes crucial to dispose of the composite materials sustainably. In this context, the proposed approach for recycling composite materials involves two main phases: the mechanical separation of flax fibers from the resin and the chemical recycling of the resin through hydrolysis.The mechanical separation involves the crushing of the composite material, which breaks down the structure and increases the contact surface area. This process facilitates the subsequent separation of fibers from the resin matrix, allowing for the recovery of flax fibers for potential reuse in other contexts. The second step of the recycling process involves the chemical treatment of bio-resin through hydrolysis. This method entails breaking the chemical bonds of the resin using water as a reactant. This disposal/recycling method enables the synthesis of new resins through the polymer materials used, thereby reducing dependence on natural resources and waste generated from hull disposal.

3.4 Foils

From our second year on, commercial foils will not be allowed in the competition, we plan to use them as training gear for our skippers and as a matter of reference for any future study.

3.5 Wings

The wings of our boat, created through the technique of upcycling, represent an innovative example of creative recycling. Upcycling involves transforming waste materials or unused items into products of higher value, without necessarily resorting to complex processes like melting. This approach is based on the idea of reducing the consumption of natural resources and environmental impact while promoting creativity and sustainability. For the realization of the wings, windsurfing masts were recovered from local sports centers. However, the disposal of carbon fiber windsurfing masts can pose complex challenges due to the intrinsic characteristics of the material. Carbon fiber is known for its lightweight and strength, but at the same time, it is non-biodegradable, making its natural decomposition difficult. Consequently, the opportunity to reuse or recycle carbon fiber windsurfing masts for different structural purposes was evaluated, provided they were still in good condition at the end of their lifecycle. Adapting the recovered windsurfing masts for alternative structural purposes may involve modifications and adjustments based on specific design requirements. However, by leveraging the flexibility and robustness of carbon fiber, remarkable and highly functional results can be achieved. This approach not only reduces the flow of waste destined for landfills but also provides a sustainable solution for maximizing the unique properties of carbon fiber.

3.6 Rig

The running and standing rigging of boats, consisting, for example, of lines, represents an essential element for sailing and controlling the sails. The lines, made of nylon, undergo a lifecycle that ultimately requires proper disposal or recycling. Considering that nylon is a recyclable plastic material, there are several options for sustainably managing nylon lines

once they reach the end of their useful life. In many coastal communities or at ports, specific recycling programs are active in recovering and recycling boat equipment and parts, including nylon ropes. These programs usually involve dismantling the boats and recovering the materials. Once dismantled, the recovered materials are collected and sent to specialized recycling facilities, where they are processed and transformed into new materials or products. The recycling process of nylon lines generally involves crushing the material and then melting it to create regenerated nylon pellets. These pellets can then be used to produce a wide range of new materials, including fabrics, pipes, and containers.

3.7 Actions for a sustainable future

Our team is committed to making the Mariposa boat sustainable, with particular attention to the choice of materials for the hull and their environmental impact. In anticipation of our first competition, we are working to develop eco-friendly solutions, focusing on researching new natural fibers and biodegradable resins for the next edition. Among the options being considered is the possibility of replacing carbon fiber with basalt fiber, considering that basalt fiber, produced from natural volcanic rocks, requires less energy for production compared to carbon fiber, making it potentially more environmentally sustainable. Additionally, we will strive to promote circular economy practices, such as material recycling and reuse. This means not only recycling and reusing materials but also designing our products with their end-of-life in mind. Encouraging the adoption of sustainable materials is another fundamental part of our approach. We are exploring the possibilities of certifications and eco-labels to help consumers identify sustainable products and services, encouraging informed and responsible choices. Finally, we have recognized the potential of 3D printing to positively influence sustainability and innovation. This technology will allow us to reduce the waste of materials and resources by producing objects only when needed and in the required quantity. Furthermore, it enables efficient use of materials, as it is possible to design optimized internal structures for strength and lightness, thus reducing material waste. This approach allows us to achieve high performance with less material, contributing to the overall reduction of our boat's environmental impact. Some 3D printing technologies allow the use of recycled or biodegradable materials. This means we can integrate materials from sustainable sources, contributing to reducing the environmental impact associated with the production of new materials.

4 TEAM

The idea was born from the desire of Dr. Eng. Flavio Stochino (Scientific Head Chief) and Dr. Eng. Gianmario Broccia (Team Manager) to instill in the students of the University of Cagliari not only theoretical notions but also practical skills of interpersonal and working nature, through the "Learning by doing " approach. Subsequently, supported by the engineering student Gabriele De Marco (Team Captain), the activities to create the team began.
In November 2023, through an email invited by Prof. Stochino to all Engineering students and subsequently through word of mouth, the project was a great success, thus selling more than several tens' people candidates to join the Team.

After a period of acquaintance and selection of the students, the team was divided into departments and sub-departments, each of which is headed by a Group Leader, who has the task of marking out the times and tasks of the various members of his department to optimize the better work.

There are 6 main departments:

1. Design.
2. Construction and maintenance.
3. Social media and image.
4. Marketing and communication.
5. LCA and materials.
6. Electronics and sensors.

4.1 TEAM MEMBERS

Prof. Flavio Stochino (Scientific Head Chief)
Gianmario Broccia (Team Manager and Coach)
Gabriele De Marco (Team Captain and Skipper)

4.1.1 Design

The design department was in turn divided into various sub-departments which, communicating closely, created the project of our prototype. The sub-departments are:

- Structural Calculation.
- 3D modelling.
- CFD simulation.
- 3D printing.

The members of the Design department:

Marta Saccone (Group Leader of the Structural Calculation department)
Alessio Vacca (Group Leader of the 3D Modelling and CFD Simulation departments)
Federico Schirru (Group Leader of the 3D Printing department)
Carlo Murru
Filippo Schintu
Pasquale Antonucci
Matteo De Curtis
Michele Chessa
Lorenzo Cui

4.1.2 Construction and maintenance

The members of the Construction and Maintenance department:

Melissa Casula (Group Leader)
Davide Cambuli
Chiara Asole (Logistics Officer)

Pietro Murru
Edoardo Bianchi
Roberta Cerciello
Francesca Pedde
Luca Vitaliano Damiano
Gian Matteo Lecis

4.1.3 Social media and image

The components of the Social media and image department:

Aurora Catalano (Group Leader and Communication officer from November to April)
Vittorio Greggio
Alessandro Zedde (Group Leader from April to July)
Edoardo Exiana (Communication Officer from April to July)
Alessio Randaccio
Anita Deplano
Laura Defraia
Chiara Maria Scanu

4.1.4 Marketing and Communication

The members of the Marketing and Communication department:

Celine Krone (Group Leader)
Eloise Acchida
Luca Montisci
Alessio Musiu

4.1.5 LCA and Materials

The members of the LCA and materials department:

Marta Saccone (Group Leader)
Melissa Casula
Chiara Asole (LCA analyst)
Davide Cambuli (LCA analyst)
Dario Frogheri
Edoardo Bianchi

4.1.6 Electronics and Sensors

The members of the Electronics and Sensors department:

Roberto Pileri (Group Leader)
Mattia Pistolesi
Federico Schirru
Luca Vitaliano Damiano

Sebastiano Mereu
Andrea Orrù

5 ACKNOWLEDGEMENTS

We would like to express our most sincere thanks to the University of Cagliari, without which all this would not have been possible. We would like to thank you for believing in our project from the beginning and for your constant support with funds, visibility, spaces, equipment, courses and more. For this reason, special thanks go to the Magnificent Rector Francesco Mola and to the Dean of the Faculty of Engineering Daniele Cocco.

Heartfelt thanks also go to all those professors who, in addition to our Scientific Head Chief, contributed to our project by making their knowledge and support available. In particular, we would like to thank Prof. Paolo Castello for his support in the electronics and sensors department, Prof. Mario Spagnulo for his support in the 3D printing sub-department, Prof. Giorgio Querzoli for his help in the sub-department CFD simulation department, Prof. Enrica Vecchi for her help with the 3D scan of the hull and foils and all the other professors who were always available.

Special thanks go to our sponsors, whose support contributed significantly to the creation of this prototype. Finding so much support in such a short time confirms that we are on the right path and motivates us to continue with commitment.

Being a team born only in November, we needed to learn several skills, including lamination. For this, we would like to thank our dear friend David Montali, who provided us with valuable lessons on the infusion of flax and carbon, sharing with us the secrets of his trade.

We would also like to thank all the students who, although not part of our team, helped us on site by dedicating their time to our goal. In particular, we would like to thank Arnas Majumder, Ryno Meintjes and Tian Meintjes for their contributions.

A special thank you goes to all the people and companies who helped us by donating pieces of broken carbon or fiberglass, such as windsurfing masts that we recycled for the construction of our Moth. We would like to thank Mauro Covre and the Polisportiva Mare Quartu, Matteo Spanu and the Wind Academy Sardinia, and Giovanni Fabbri for their valuable contribution.

Finally, we would like to thank Federico Meloni Hernandez for donating us the mold of the Manta Moth V1, which, although it had reached the end of its useful life, we were able to save from the garbage and reuse for the creation of our boat.

6 SPONSORS

UNICA
UNIVERSITÀ
DEGLI STUDI
DI CAGLIARI

7 MARINESHIFT 360 LCA

The theme of sustainability is a topic that is close to the heart of the Unica Sailing Team. Despite being the first year and the short time available, our team is committed to breaking down the ecological footprint of the realization and production of the boat. To accomplish this task, we have used the MarineShift360 software to quantify the life cycle assignment of the materials used. Although we have maintained certain techniques of industrial production, we have tried to exploit to make the most of the upcycling technique by making a damaged material or element a resource for our project. Our goal for years to come is to reuse many of the components produced this year for the first time to reduce the environmental impact more and more.

7.1 General results

Here some graphs summarize a part of the work that has been done.

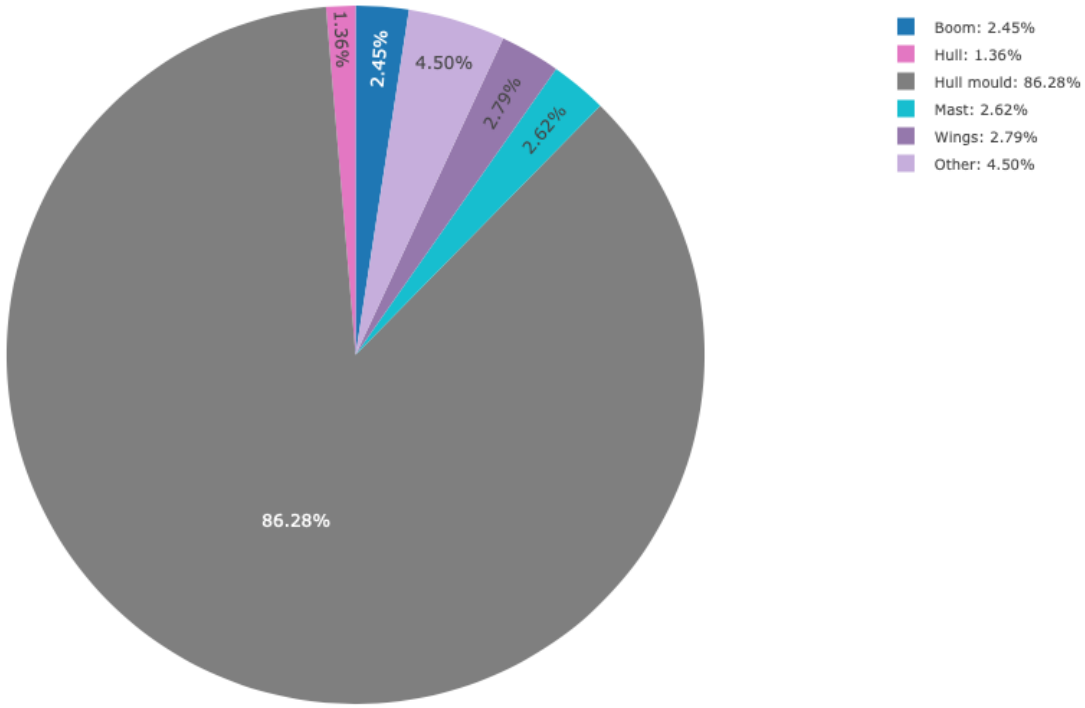

Figure 719: Energy consumption – non renewable

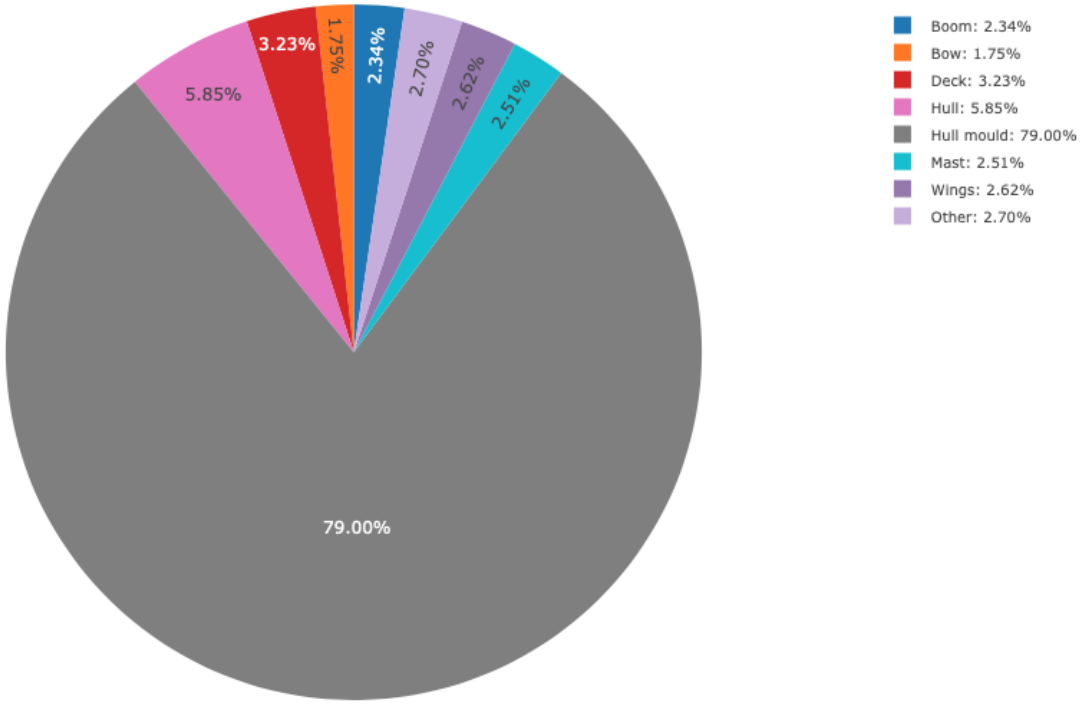

Figure 60: Energy consumption – renewable

As can be seen from the graphs regarding the electricity consumed, more than 79% of the energy was used to produce the mold that was not produced directly by us. We would like to point out that the mold we used should have been thrown away as it was no longer in use, despite the very good condition it was in. Our goal is to continue to use the same mold to produce the subsequent Moth, fully marrying the philosophy of upcycling and not waste. The total of the non-renewable energy used was, unfortunately, higher than renewable energy, the first was 120,16k (MJ) while the latter was 11.87k (MJ).

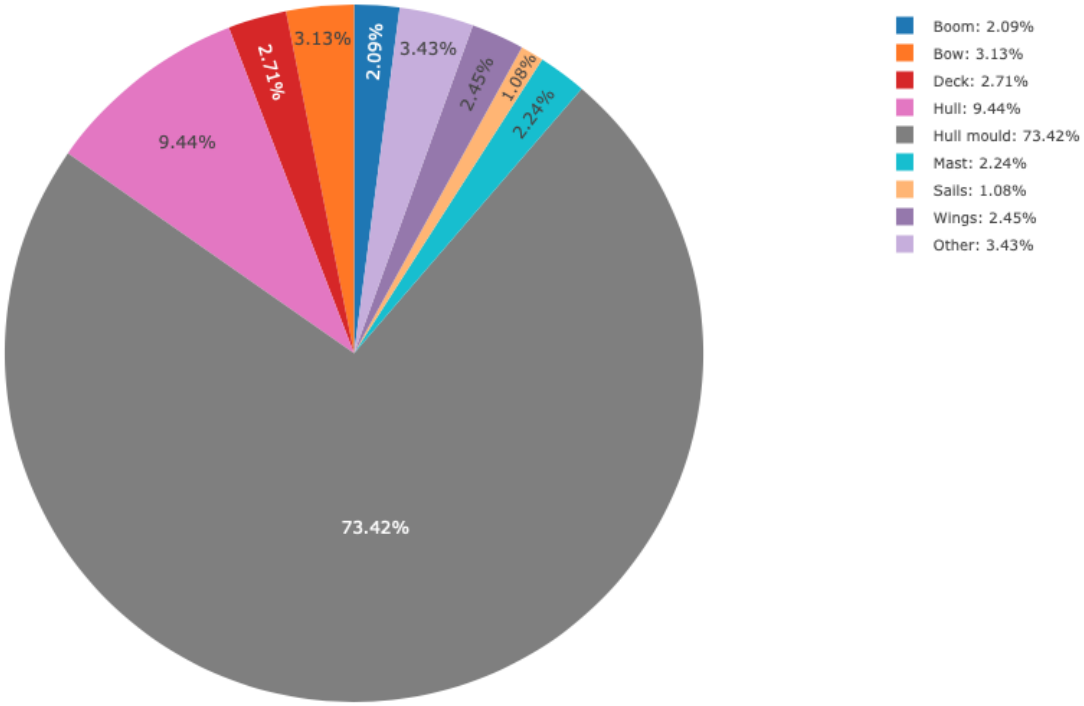

Figure 61: Water consumption

The graph, Figure 61 shows the water consumed to produce the materials or during a specific process, which in our case mounts at 77,06 m^3. The use of flax fiber has led us, as a result, to a greater consumption of water. For the hull and deck, we used a layer of twill UD 220gr/m^2, two layers of biaxial flax fiber (+-45°) 250gr/m^2, and a layer of 230gr/m^2 Power Ribs. Despite this, the presence of the hull mold in the graph is still predominant.

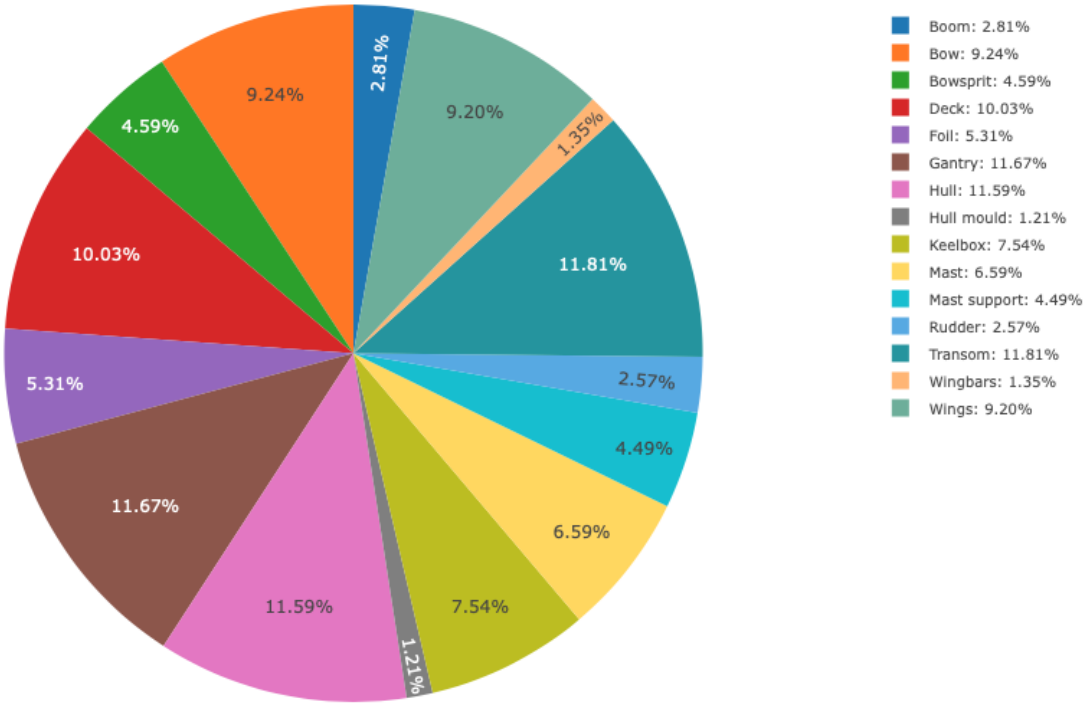

Figure 62: Waste factor

The pie chart shown here represents the weight ratio of (ordered material + auxiliary material) – final material / (ordered material + auxiliary material) which in our case was 12,14% of the total. The ability to use different techniques has allowed us to minimize the waste factor according to the necessary process. It is possible to notice that techniques such as infusion have a higher percentage than hand rolling, this is an important fact to optimize processes as needed and to learn which methods help us reduce the waste factor.

7.2 APPENDIX A - MS360 LCA

7.1.1. Boat life cycle assessment discussion

The MarineShift360 software was used during construction to obtain feedback at various project stages. The available options left us satisfied, as the software proved to be quite comprehensive and user-friendly even for beginners. The calculations helped us quantify the auxiliary materials used. During the construction phase, we aimed to optimize these auxiliary materials, successfully reducing the overall impact thanks to the software's quantifications. Being our first year, many components used will continue to be utilized in the future, aligning with the recycling and upcycling philosophy as much as possible.

7.1.2 Boat life cycle assessment scheme

Referring to section 3.1, through a detailed analysis of the components and processes involved in its creation, we were able to identify the key components contributing to the overall impact, such as:

- Boom

- Hull
- Bowsprit
- Deck
- Foil
- Gantry
- Hull mould
- Keel box
- Lines
- Mast
- Mast support
- Rudder
- Sail
- Transom
- Wings

A.2. Overall results & CO2 equivalent impact

Below are the diagrams illustrating the remaining results obtained and the CO2 equivalent impact. For further information and comments, please refer to Section 7 of the report.

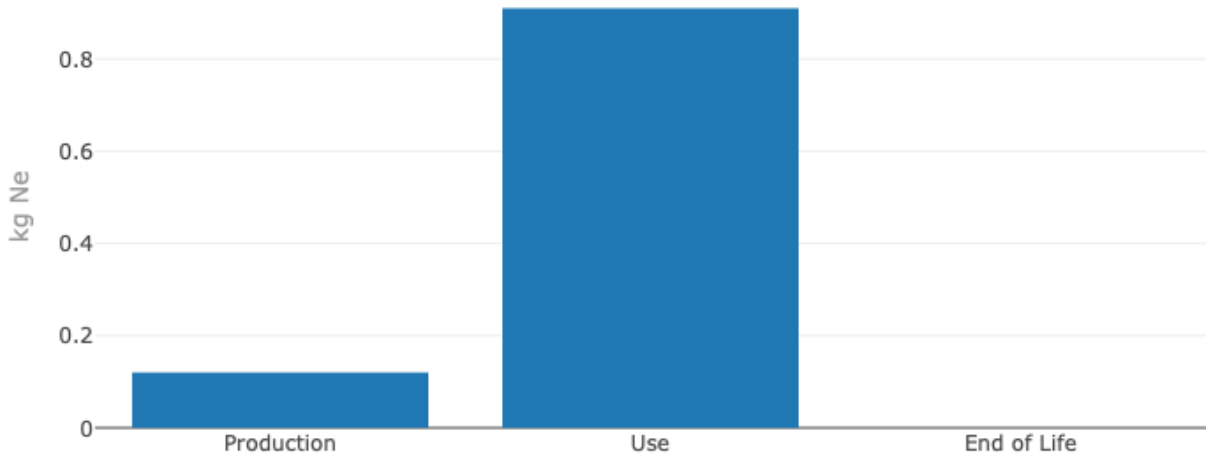

Figure 72: Marine Eutrophication

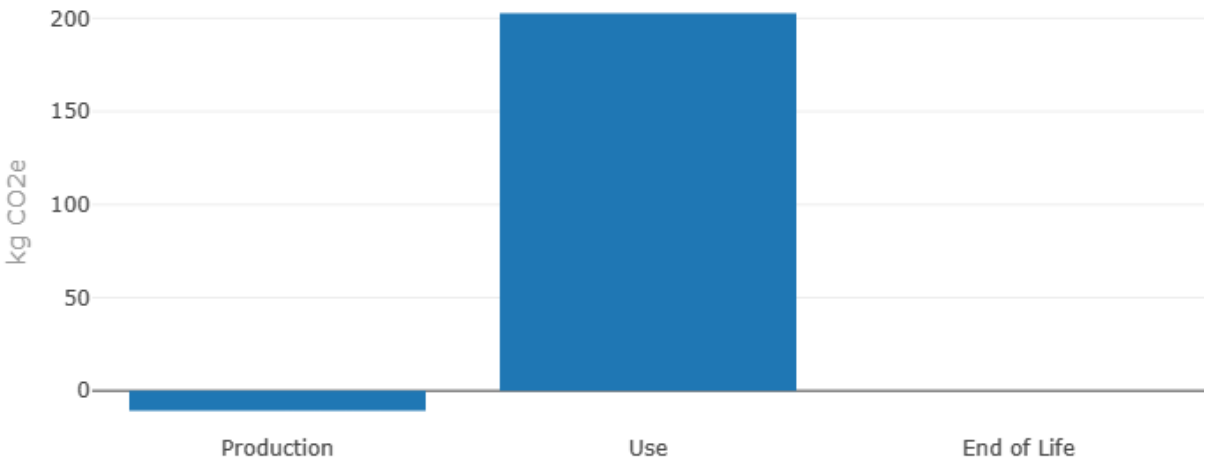

Figure 73: Global warming – non fossil

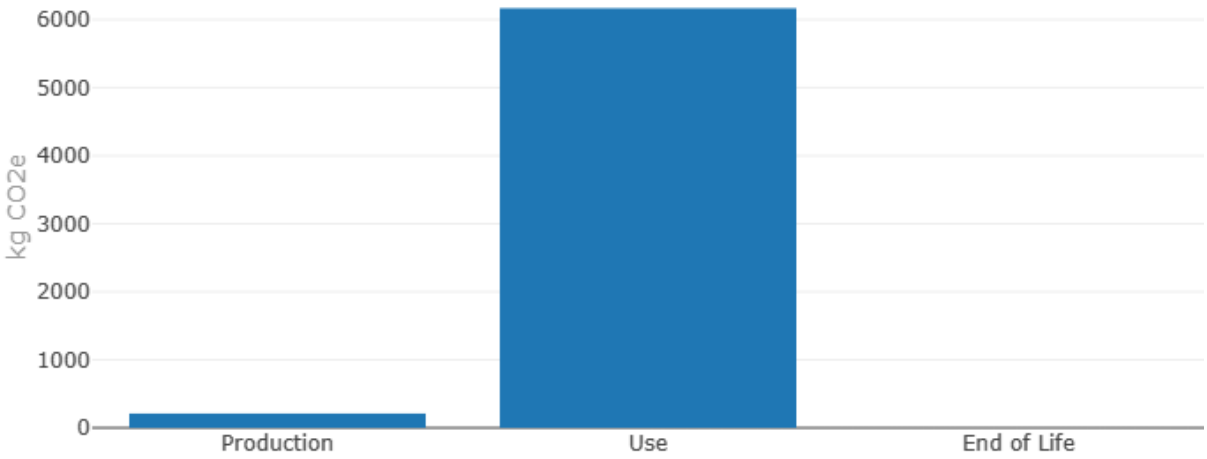

Figure 74: Global warming – fossil

8 BIBLIOGRAPHY

1. *Composite Laminate Analysis Spreadsheet.*
2. NordCompensati. *Dati tecnici.*
3. Hoorn, Philip van. *High-Performance Sailing Aerodynamics.* Chalmers : University of Technology, 2021.
4. Gaudio, R. Miglio, R. and Dey, S. *"Nonuniversality of von Kármán's κ in fluvial streams".* s.l. : Journal of Hydraulic Research, International Association for Hydraulic Research (IAHR), Vol. 48, No. 5, 658-663, (2010).
5. OpenFOAM. *User Guide: simpleFoam.*
6. EasyComposite. *Carbon fiber mechanical properties.*